MR. LUCAS VIMPERE (Orcid ID : 0000-0001-9315-1243)
MR. NICOLÒ DEL PIERO (Orcid ID : 0000-0002-5290-7355)

Article type : Original Manuscript

Upper Pleistocene parabolic ridges (i.e. 'chevrons') from the Bahamas: Storm-wave sediments or aeolian deposits? A quantitative approach

Lucas Vimpere[1], Nicoló Del Piero[1], Nabil Shawwa[2], Karim Beguelin[1], Pascal Kindler[1], Sébastien Castelltort[1]

[1]Department of Earth Sciences, University of Geneva, Rue des Maraîchers 13, 1205 Geneva, Switzerland

[2]Department of Earth Sciences, Carleton University, 1125 Colonel by Drive, Ottawa, ON K1S 5B6, Canada

Associate Editor – Massimiliano Ghinassi

Short Title – Bahamian parabolic dunes (i.e. 'chevrons')

ABSTRACT

The Upper Pleistocene (Marine Isotope Stage 5e; *ca* 120 ka) stratigraphic record from the Bahamas comprises large, kilometre-long parabolic ridges of oolitic composition, that point landward, and have been up to now called 'chevrons'. A debate about their genesis has led previous researchers to consider two processes of deposition: (i) a catastrophic event involving giant storm-generated waves produced by specific climatic conditions at the end of Marine Isotope Stage 5e; and (2) a more uniformitarian process which characterizes 'chevrons' as aeolian parabolic dunes because of their similar morphology. Since there are few unequivocal sedimentological criteria to discriminate aeolian from water-deposited sediments, only a

quantitative, multi-method approach could provide enough evidence to produce a viable diagnosis on the genetic processes involved. Following this reasoning, the quantification of the morphological parameters of 'chevrons', a precise study of their sedimentary structures on previously and newly discovered sections, and several statistical grain-size analyses, all advocate for an aeolian origin. Moreover, when the aforementioned characteristics of 'chevrons' are compared with those of storm deposits (for example, washovers) and parabolic dunes occurring elsewhere on Earth, the dissimilarity with the former and the resemblance with the latter is evident. Amino-acid racemization dating, together with stratigraphic and petrographic investigations, constrain the age of the 'chevrons' to the late part of Marine Isotope Stage 5e. Their occurrence during this specific time interval can be explained by both strengthened easterly winds and drier climatic conditions associated with changing vegetation cover. Fixation of the arms by sparse vegetation, coupled with the loose 'chevron' nose sediment migrating farther inland, form the peculiar U-shaped morphology of these ridges.

INTRODUCTION

Up to now called 'chevrons', the peculiar V-shaped and U-shaped oolitic ridges of Late Pleistocene age exposed on several Bahamian islands have drawn the attention of numerous researchers for almost two decades (Bourgeois & Weiss, 2009; Donovan & Tormey, 2015; Engel *et al.*, 2015; Hansen *et al.*, 2020, 2016, 2013; Hearty *et al.*, 2015, 2002, 1998; Hearty & Tormey, 2018a, 2018b, 2017; Kindler & Strasser, 2002, 2000; Mylroie, 2018a, 2018b; Rovere *et al.*, 2018, 2017; Tormey, 1999; Tormey *et al.*, 2018, 2016; Tormey & Donovan, 2015; Vimpere *et al.*, 2019). However, despite the numerous studies pertaining to these landforms, both their formation mechanism and their climatic significance remain uncertain and controversial. Two conflicting hypotheses have so far been proposed: (i) Hearty *et al.* (1998) first suggested that large, long-period waves generated by distant 'superstorms' dumped sediments in a hairpin form onto the islands at the end of the substantially warmer Last Interglacial period (LIG; Marine Isotope Stage 5e; 126 to 113 ka BP; Thompson *et al.*, 2011); and (ii) by contrast, Kindler & Strasser (2002, 2000) inferred a wind-driven formation process for these deposits because of the number of similarities between 'chevrons' and aeolian parabolic dunes.

The first assumption concurs with the so-called 'ice-surge hypothesis' (DeConto & Pollard, 2016; Hansen *et al.*, 2016; Hollin, 1965; Mercer, 1978; Neumann & Hearty, 1996; Wilson, 1964), which portrays a rapid transgression and catastrophic climatic changes at the end the LIG linked to a collapse of Antarctic ice sheets. These events would have facilitated the formation of giant waves by chain-reaction, notably by strengthening pressure, temperature and moisture gradients adjacent to warm tropical waters (Hearty & Neumann, 2001). Hearty *et al.* (2002, 1998) and Hearty & Tormey (2017) further identified a 'trilogy' of field evidence for long-period wave deposits in the Bahamas: (i) the 'chevrons', which accumulated in lowland areas under this morphology because of the rapid loss of wave kinetic energy; (ii) seven 'megaboulders', up to 2000 tons in weight, some of which stand on top of a 20 m high cliff at one location in Eleuthera; and (iii) stacked, seaward-dipping 'run-up' deposits including scour structures and 'rip-up' breccias. The occurrence of fenestral porosity in both 'chevrons' and 'run-up' deposits is presented as additional evidence of a wave-induced origin for these landforms because fenestrae (i.e. keystone vugs) are commonly associated with wave-swash action (e.g. Dunham, 1970).

The second hypothesis relies on the morphological resemblance between aeolian parabolic dunes and 'chevrons' (Engel *et al.*, 2015; Kindler & Strasser, 2002, 2000) and on the alignment of the latter with the present resultant drift direction of carbonate sand generated by north-easterly winds (Vimpere *et al.*, 2019). The occurrence of rhizoliths, land snails and the omnipresence of climbing translatent stratification (CTS) within 'chevrons' and 'run-up' deposits further argues for an aeolian origin, because these fine structures are by and large considered as diagnostic of wind processes (Caputo, 1993; Frébourg *et al.*, 2008; Fryberger & Schenk, 1988; Hunter, 1977; Loope & Abegg, 2001; Loucks & Ward, 2001; McKee & Ward, 1983; White & Curran, 1989). In this hypothesis, fenestral pores are interpreted as resulting from the effect of rainfall. This formation process has been observed in modern coastal dunes (Emery, 1945; Frébourg *et al.*, 2008) and in a subaerial dam spillway (Stieglitz & Inden, 1969), and also reproduced experimentally (Bain & Kindler, 1994). Fenestrae have also been described from aeolianites of Holocene (Engel *et al.*, 2015; Loucks & Ward, 2001) and Pleistocene age (Bain & Kindler, 1994; Frébourg, 2010). Finally, the morphological and sedimentological disparities between well-identified storm deposits (for example, washover lobes and conglomeratic berms) and 'chevrons' (Engel *et al.*, 2015; Kindler & Strasser, 2002, 2000; Mylroie, 2018a, 2018b; Vimpere *et al.*, 2019) do not agree with a wave origin for the latter. Regarding the 'megaboulders', Rovere *et al.* (2018, 2017) used a wave model to demonstrate the needlessness of evoking 'superstorms' as an emplacement mechanism when hurricanes of historical intensity can transport boulders of such sizes. Because of their geographically limited distribution, Mylroie (2008) proposed a cliff-rollback model (boulders rolling down from the cliff edge to overlie a younger unit), which was discussed as the best option by peers (Hasler *et al.*, 2010; Kindler *et al.*, 2010; Viret, 2008).

This study provides new quantitative data on the morphology, sedimentology, granulometry and timing of deposition of 'chevrons' from the islands of Eleuthera, Long and Great Exuma. 'Chevrons' from Acklins Island were only considered for remote measurements because no field data have been collected there. This study aims to resolve the controversy regarding the formation and the significance of these landforms. Figuring out whether these Upper Pleistocene V-shaped and U-shaped ridges from the Bahamas result from large-storm action or from aeolian

processes is certainly of importance in the present-day context of anthropologically induced global climatic changes and sea-level rise.

SETTINGS

Geographical settings

Located to the East of Florida and to the North of Cuba, the Bahamian archipelago is composed of a series of isolated, flat-topped carbonate platforms extending for more than 1000 km along a north-west/south-east axis. This study concerns three islands situated on the Great Bahama Bank (GBB; Eleuthera, Great Exuma and Long) and Acklins, which is located on the Crooked-Acklins Bank to the South of GBB (Fig. 1). The area was long considered as slowly subsiding in a tectonically stable context (Carew & Mylroie, 1995a; Lynts, 1970; Mullins & Lynts, 1977), but this tectonic stability has recently been questioned (Kindler *et al.*, 2011; Mulder *et al.*, 2012). Most of the islands are elongated and narrow in shape (Fig. 1), and essentially composed of a complex 3D arrangement of wind-blown carbonate sediments of Quaternary age. High-energy conditions along the Atlantic coastlines and quiet lagoonal environments on the bank side lead to sediments being mostly transported from east to west, parallel to the constantly blowing easterlies.

Present-day and last interglacial climate in the Bahamas

The Bahamas are located in the tropical monsoon climate zone, as defined in the Köppen classification, and experience two main seasons largely determined by the movements of the Intertropical Convergence Zone (ITCZ). In the winter, the southward motion of the ITCZ induces temperate–warm, dry and windy conditions over the archipelago, whereas in the summer its northward shift results in a hot and humid climate with weaker trade winds (Kottek *et al.*, 2006; Peel *et al.*, 2007). The Bahamian climate is mostly influenced by the latitudinal extension of the archipelago, which leads to a climatic heterogeneity between the northern and southern part. Indeed, whilst temperature is rather constant throughout the archipelago in the summer, it is clearly warmer in its southern part in the winter (Sealey, 2006). Moreover, the average yearly rainfall is 850 mm, but regional variations range from 700 mm to 1500 mm/yr (Wolcott *et al.*, 2018), the southern part of the archipelago being much drier than the northern part.

The LIG is commonly known as one of the warmest interglacial periods of the last 800 kyr (Past Interglacials Working Group of PAGES, 2016) with a global average temperature estimated at 1.5

to 2.0°C warmer than the pre-industrial one (Hansen *et al.*, 2016), and a sea level rise of 6 to 9 m above the present one associated to significantly reduced ice sheets (Dutton *et al.*, 2015). As such, it has been used as a potential analogue for future climate models (Hansen *et al.*, 2020; Masson-Delmotte *et al.*, 2013). Prolonged anomalies of the ITCZ position have long-term effects on the climatic conditions in the tropics, which have been linked with changes in sea surface temperature (SST) and salinity (SSS), Atlantic Meridional Overturning Circulation (AMOC) and ice sheets extent (Gibson & Peterson, 2014; Hoffman *et al.*, 2017; Peterson & Haug, 2006; Zhuravleva & Bauch, 2018). In the Bahamas, a southward shift of the mean annual position of the ITCZ is usually related to cooler and drier stadials with intensified trade winds, whereas a northward shift is linked to higher temperatures, increased precipitation and weakened trade winds. By studying faunal assemblages, the isotopic signal and X-ray fluorescence (XRF) data, Zhuravleva & Bauch (2018) advocate a warm/humid and cooler/drier early/late MIS 5e, respectively, which correlates with the SST being higher during the early MIS 5e than during the late MIS 5e (Hoffman *et al.*, 2017). These authors also determined that a sudden southward displacement of the ITCZ at around 127 ka BP interrupted a warm phase in the early part of MIS 5e and induced an abrupt 'Younger Dryas-like event'.

Last interglacial stratigraphy and sea-level history of the Bahamas

The studied V-shaped or U-shaped ridges belong to the Grotto Beach Formation (GBF), which has been correlated to the LIG. The GBF generally overlies the Owl's Hole Formation (Carew & Mylroie, 1985; Fig. 2), which comprises both bioclastic and oolitic–peloidal calcarenites of Middle Pleistocene age (Hearty & Kaufman, 2000; Kindler & Hearty, 1996). It is capped either by bioclastic aeolianites generally correlated to MIS 5a (Almgreen Cay Formation, Hearty & Kindler, 1993; Whale Point Formation, Kindler *et al.*, 2010) or by the Holocene Rice Bay Formation (Carew & Mylroie, 1985), which includes: (i) oolitic–peloidal aeolianites (North Point Member, Carew & Mylroie, 1985); and (ii) a shallowing-upward succession of mostly bioclastic sediments deposited in beach to dune environments (Hanna Bay Member, Carew & Mylroie, 1985). The GBF comprises three members (from base to top):

The *French Bay Member* (FBM; Carew & Mylroie, 1985) consists of a well-preserved oolite showing sedimentary structures typical of the subtidal, intertidal and mostly the aeolian depositional environments (e.g. Caputo, 1995). It can be correlated with the early part of the LIG

based on its position relative to the well-dated overlying unit (see below) and amino-acid racemization (AAR) data (Hearty & Kaufman, 2000). The FBM has been interpreted as transgressive-phase aeolianites of the GBF (Carew & Mylroie, 2001, 1995b, 1985), or as deposits corresponding to a distinct highstand at the beginning of MIS 5e (Hearty & Kaufman, 2000; Hearty & Kindler, 1993; Kindler & Hearty, 1996).

The *Cockburn Town Member* (CTM; Carew & Mylroie, 1985) comprises coral boundstone/rudstone and shell-rich floatstone corresponding to ancient reefal and lagoonal settings, respectively. The reefal facies is particularly well-represented in Mayaguana (Godefroid, 2012) and Great Inagua (Skrivanek *et al.*, 2018; Thompson *et al.*, 2011). Uranium–Thorium (U-Th) ages from well-preserved coral samples range between 130 ka and 116 ka BP (Chen *et al.*, 1991; Kindler *et al.*, 2011; Thompson *et al.*, 2011), allowing correlation with MIS 5e.

The *Fernandez Bay Member* (Hearty & Kindler, 1993), or *Boat Cove Member* (Godefroid, 2012), corresponds to a shallowing-upward succession of oolitic to bioclastic sediments deposited in subtidal, intertidal and aeolian environments, and it conformably overlies the CTM. It can be correlated with the late part of the LIG because of its position above the CTM, and because of AAR data (Hearty & Kaufman, 2000). This succession possibly records a distinct sea-level highstand at the end of MIS 5e (Hearty & Kaufman, 2000; Hearty & Kindler, 1993; Kindler & Hearty, 1996), but can alternatively be interpreted as the regressive-phase deposits of the GBF (Carew & Mylroie, 1995b, 1995a, 1985). Considering the uncertainties pertaining to sea-level history during the LIG (e.g. Barlow *et al.*, 2018), this specific point remains an open question.

METHODS

Morphology

To quantify the specific morphological parameters of 'chevrons', a Digital Elevation Model (DEM) of the Bahamas generated by the satellite TanDEM-X and provided by the German Aerospace Centre (DLR) was used. The product is a grid given at 0.4 arcsec at the equator (*ca* 12 m) with absolute horizontal (AHA) and vertical (AVA) accuracies (respectively expressed as a circular and linear error at 90% confidence level) higher than 10 m. The relative vertical accuracy (RVA) is about 2 m for a slope ≤20% and about 4 m for a slope >20% (Wessel *et al.*, 2018). The length (L), width (W), height (H), stoss-slope angle (φ), slip-face angle (α), L/W and L/H ratios were

measured (Fig. 3; Appendix 1) on 10 'chevrons' located on three of the studied islands: Great Exuma, Long and Acklins. The collected data were then compared with those measured on 95 aeolian parabolic dunes, located in nine countries (Australia, Brazil, Denmark, Libya, The Netherlands, Scotland, Spain, USA and Wales) and covering the tropical, subtropical and temperate zones worldwide (Appendix 2). The same global DEM was used for parabolic dunes measurements. Following the methodology used by Yan & Baas (2017), *L* expresses the average longitudinal distance between the front of the apex and the tips of the arms:

$$L = {}^{1}/_{2}(L_1 + L_2)$$

W is the average dune width between the tips of the arms and the lobe, obtained from at least five measurements:

$$W = \sum_{i=1}^{n} {}^{W_i}/_{n}$$

The estimations of sand volumes were made by calculating the pile volume defined by computing sample elevations along the perimeter of the ridge. By assembling these elevations, a terrain surface was generated that represents the 'chevron' base and enabled calculation of its volume. Since 'chevrons' lie on lowlands, the possibility of having an older substrate forming reliefs below their base is negligible as well as the uncertainty on the sand volume.

Field method

After recognition of the 'chevrons' on the DEM, satellite and drone images were scrutinized to find potential roadcuts or sections exposing their nose part. Sedimentary structures were examined in detail at every exposure. Each dip value of large-scale cross-beds is a calculated average of 20 values taken in the field. Small-scale sedimentary structures were described following the classification developed by Hunter (1977) in siliciclastic deposits and adapted to carbonate rocks by Loucks & Ward (2001). Following their classification, the term bounding surfaces is applied here to describe truncation surfaces of different orders of magnitude. First-order bounding surfaces are the most extended, cut across cross-bedding and other dune

structures, and are often associated with the development of a protosol. Thus, they represent long-term exposure surfaces and are labelled as such. Second-order bounding surfaces are less extended, bound sets of cross-strata and are truncated by the first order bounding surfaces. Therefore, they illustrate short-term reactivation surfaces that may correspond to short stops in the sedimentation or to a change in the wind direction. Particular attention was paid to the occurrence of three stratification types: (i) *climbing translatent stratification* (CTS), which consists of millimetre-thin, inversely graded laminae generated by the migration of wind ripples across the dune; (ii) *grainfall lamination,* which corresponds to millimetre to centimetre-thick laminae produced on the lee side of dunes where flow separation occurs; and (iii) *sandflow cross-stratification* that forms centimetre-thick, lens-shaped laminae resulting from sand avalanching on the dune slip face.

Comparative microfacies analyses

Oriented samples collected in the field (n = 147) were cut, impregnated with blue epoxy, thin-sectioned and then analysed under a Zeiss axioscope petrographical microscope (Carl Zeiss Microscopy, Oberkochen, Germany) connected to a Leica dfc 450c camera (Leica Microsystems, Wetzlar, Germany) to ascertain their composition, diagenetic alteration and micro-sedimentary structures such as CTS.

To further clarify the depositional process at the origin of 'chevrons', the granulometry of these landforms was compared by image analysis to that of well-identified, *coeval* aeolian and beach deposits. Samples were taken from foresets, topsets and backsets, as well as from planar, wedge-planar and trough cross-beds to avoid representativity bias. Image analysis requires high-resolution scans of thin sections (4000 dpi), which were acquired using a Nikon Super Coolscan 4000 (Nikon, Tokyo, Japan). Grain-size investigation was performed by manually measuring in two-dimensions the long-axis diameter of 250 grains per section, using a random grid automatically generated in the image-analysis software *JMicroVision* (Roduit, 2007). This type of grid prevents potential uncertainties generated by a recursive (i.e. regular) one not suited to the mean grain size (Neilson & Brockman, 1977), although the homogeneous character of the studied oolitic deposits avoids any over-representation of large or small particles. The nature of ooids and peloids, being spherical or ovoidal well-rounded carbonate grains, makes the

underestimation of a particle diameter generated by the random nature of the section negligible (Higgins, 2000).

The computation of grain-size statistics was done with GRADISTAT v.8 (Blott & Pye, 2001), which is an Excel® macro that provides a rapid calculation based on the mathematical 'method of moments' (Friedman & Johnson, 1982; Krumbein & Pettijohn, 1938) and the method of Folk & Ward (1957). It uses both metric and logarithmically transformed scales ($\phi = -\log_2(d)$; where d is the grain diameter), with the same number of classes as the ones proposed by Friedman & Sanders (1978), but with a slightly modified nomenclature (Appendix 3). Calculated parameters include the mean grain size, sorting, skewness, kurtosis and seven different cumulative percentile values (D_{10}; D_{50}; D_{90}; D_{90}/D_{10}; $D_{90} - D_{10}$; D_{75}/D_{25} and $D_{75} - D_{25}$).

Amino-acid racemisation dating

In the Bahamas, amino-acid racemization (AAR) chronology has successfully been used to date whole-rock samples and shells of terrestrial gastropods (e.g. Hearty, 2010; Hearty & Kaufman, 2009, 2000; Hearty & Kindler, 1993; Hearty & Schellenberg, 2008). This rapid and inexpensive method commonly provides a reasonable time frame of targeted periods of deposition. Avoidance of possible biases in AAR data was ensured by carefully sampling 'chevrons' away from any alteration source and soil (>1 m from the surface). Samples for AAR analysis were collected from grainfall and grainflow laminae in nose sections and from CTS beds in the arm sections.

Four whole-rock 'chevron' samples were cleaned until there was no more crust or bacterial mats left to limit the contamination of the supposedly closed amino-acid system by oxidised or externally derived material (Walker, 2005). This operation was made with a small stainless-steel chisel. Then, the samples were powdered to a size comprised between 250 µm and 1 mm. This powdering was performed in a mortar with a pestle, both made of agate, to avoid any type of contamination. It was done softly to prevent any possible warming up of the sample in order to keep a realistic ratio of amino acids (Hollin *et al.*, 1993; Miller & Brigham-Grette, 1989). Once the samples were powdered, particle sorting was done by dry sieving to constrain the desired range of sizes. Finally, knowing that further procedures would use dilute HCl to remove 30% of the sample mass to reduce the possibility of contamination by cements and organic residues on grain surfaces, a minimum weight of powder of 50 g was chosen. Samples were sent to the Amino Acid

Geochronology Laboratory of the Northern Arizona University where the amino-acid content was measured by reverse phase high-performance liquid chromatography (Kaufman & Manley, 1998; Whitacre *et al.*, 2017). The D/L-glutamic-acid (Glu) ratios were found to be the most appropriate ratios (Hearty & Kaufman, 2009; Rutter, 1985; Rutter *et al.*, 1979) to date oolitic sediments, and are the only ones used in this study. The conversion method of Whitacre *et al.* (2017) was applied to the present data to calculate the Alloisoleucine/Isoleucine (A/I) values in order to compare them with the database generated in the Bahamas (Hearty & Kaufman, 2009, 2000).

RESULTS

Morphology

'Chevrons' description

The series of ridges located in the vicinity of North Eleuthera Airport do not meet the essential V-shaped or U-shaped morphology to qualify as 'chevrons'. Indeed, the two sections supposedly exposing 'chevron' arms (ELI and EAJ; Hearty *et al.*, 1998; Hearty & Tormey, 2017; Tormey, 1999) cut across distinct linear ridges that are parallel and, respectively, perpendicular to the north-west/south-east trending Atlantic shoreline (Fig. 4A). These straight-lined hills form the western and southern limits of a subdued area where an array of smaller, WNW–ESE oriented ridges occurs. Similarly, the 'chevron' located to the North of Rock Sound Airport in South Eleuthera consists of two rectilinear, parallel, WSW–ENE trending ridges that stretch from the Atlantic coast to the lagoon shoreline (Fig. 4B). Consequently, the alleged Eleuthera 'chevrons' will not be further described as such in the following chapters. On Great Exuma, the 'chevrons' are mostly concentrated in the Steventon – Farmer's Hill area (northern part of the island; Fig. 5A), where they form several nested sets. A smaller, immature but well-defined one occurs near Michelson (southern part of the island; Fig. 5B). Its arms are connected to a breached ridge, which is parallel to the shore. On Long Island, well-identified, elongated, and narrow 'chevrons' essentially occur along the Atlantic coast in the central and northern part of the island (Fig. 5C and D; Appendix 4). Finally, the U-shaped landform observed on Acklins Island is strongly asymmetrical with the north-west arm being much shorter than the south-east one (Fig. 5E).

Morphological parameters of 'chevrons' (Appendix 1)

The Bahamian 'chevrons' are mostly kilometre-scale landforms, ranging from 0.4 to 3.0 km in length (average = 1.6 ± 0.78 km) and from 0.3 to 1.2 km in width (average = 0.6 ± 0.28 km). They are low-lying deposits between 7 m and 33 m high. The mean ratios of these parameters give L/W = 2.68 ± 1.43; L/H = 112.31 ± 76.03 and W/H = 43.12 ± 19.97. They represent consequent volumes of transported sand with a pile volume (see *Morphology* section) averaging at 4.97 ± 3.10^6 m^3. Measurements show the typical difference between a steep lee face (11 ± 2°) and a gentle stoss face (2 ± 1°), which characterizes sediment bodies deposited under a unidirectional flow.

Morphological parameters of aeolian parabolic dunes (Appendix 2)

Parabolic dunes (Fig. 6), like 'chevrons', are mostly kilometre-scale bedforms, ranging from 0.1 to 5.6 km in length (average = 1.07 ± 1.03 km) and from 0.04 to 3.2 km in width (average = 0.38 ± 0.42 km). They show a high variability of height, going from 4 to 90 m and averaging at 29 ± 19 m. The different ratios of these parameters display a high variability: L/W 3.03 ± 1.52; L/H = 47.18 ± 38.11 and W/H = 17.59 ± 15.64. The typical parabolic dune displays a consequent volume of 6.94 ± 22.10^6 m^3. Once again, the difference between the lee (18 ± 9°) and the stoss face (6 ± 5°) is evident with these measurements.

Sedimentology

Sedimentary structures

The 'chevron' arms are asymmetrical in cross-section with the outer flank slightly steeper than the inner one (Fig. 7), and mostly composed of low-angle, tabular-planar cross-beds that show a concave-downward aspect towards the edges of the ridge, perpendicular to its main axis (Fig. 8A and B). When the ridge is elongated, the arms present steep foresets (Fig. 8C) that are dipping towards the outside, perpendicular to the main ridge axis. It is common to find shallow trough cross-beds cross-cutting other cross-bed sets, mostly near the top of the ridge where they meet topsets or backsets. The sets are composed of either symmetrical or asymmetrical laminae. Front-lobe exposures (Fig. 8D and E) reveal decimetre to metre-thick, tabular to wedge-shape sets of landward-dipping, high-angle cross-strata (dip value up to 30°) that can undeniably be identified as foresets. Indicators of pedogenesis such as rhizoliths, land-snail shells (*Cerion* sp.) and protosols are common within the studied 'chevrons'. Whatever the nature of the section and

the part of the ridge observed, extensive millimetre to centimetre-scale laminae were encountered at every outcrop and can be classified in three groups:

1 In the arm sections, most of the observed laminae do not show an erosional base and follow the pre-existing topography as tabular sets of strata, qualifying as grainfall laminae (Fig. 9A). They locally separate sandflow cross-stratification (Fig. 9B), occurring on the outer flanks of the arms, but are barely visible due to the small difference in grain size. By contrast, the grainfall–sandflow alternation is well-preserved and often displayed in the nose sections, especially at the front lobe toe (Fig. 9C).

2 Due to the steepness of the exposures (i.e. roadcut walls), the lenticular shape of sandflow cross-strata is generally not visible. However, these structures occur in a few sections that cut across the 'chevron' slip faces. They are enhanced by grainfall laminae, which are more competent (i.e. cemented) and show sharp, straight basal contacts dipping at high angles (20 to 30°). Grainflow and grainfall stratification are usually observed in their tabular shape but can be found wedging out into bottomsets when the base of the foresets is exposed. In aeolianite foresets, slump sandflows sometimes form high-angle asymmetrical folds in their lower part (Fig. 9D; McKee, 1966; Mckee & Bigarella, 1972; Pye & Tsoar, 2008).

3 By contrast, CTS are *ubiquitous* in the studied arm sections (Fig. 9A) and locally present in front-lobe sections where they interfinger with grainfall lamination and sandflow cross-strata. Their relief is enhanced due to the preferential cementation of the finer part of the inversely graded lamina, which tends to retain pore water more easily because of its high surface tension (Fryberger & Schenk, 1988). The CTS are commonly associated with decimetre-thick fenestrae-rich beds, which may be capped by highly cemented laminae (Fig. 9A). Fenestrae are particularly abundant in the 'chevron' arms and have been observed at elevations up to 30 m above sea level.

Petrography

The bulk of the investigated deposits consist of pure oolitic to peloidal grainstones (Fig. 10). Ooids show different stages of vadose diagenesis that are primarily controlled by their original mineralogy and the packing of the tangential needles forming the cortices (Loucks & Patty, 2017). The major process affecting these grains is the recrystallization of aragonite and high-Mg calcite into low-Mg calcite with a partial leaching initially affecting the cortices. The rare bioclasts mostly include *Homotrema sp.,* red algae and *Halimeda* sp. (Fig. 10). All carbonate grains

originated in the ocean and were washed onto the beach, from where they were transported to form the observed subaerial bedforms.

Grainfall laminae form thin levels of fine-grained, well-sorted sand, usually well-cemented. Sandflow laminae are thicker, coarse-grained, poorly sorted and poorly cemented layers alternating with the thinner grainfall laminations (Fig. 10A). Both are delimited by an abrupt change in grain size. The CTS are also delimited by abrupt changes of grain size but usually form laminae of equal thickness that show an internal inverse grain-size gradient (Fig. 10B). A differential cementation within a lamina, between a highly cemented basal unit and a poorly cemented upper unit, may resemble grainfall and sandflow, respectively. In both cases, low-Mg isopachous and pore-filling blocky cements develop in the fine-grained layers whereas low-Mg calcite, with meniscus and pendant geometries, cement the coarser-grained layers (Fig. 10A and B). This vadose cementation is by far the dominant type observable in 'chevrons' (Fig. 10F) and aeolianites. In contrast to 'chevrons' and aeolianites, beach to subtidal deposits do not show such a clear lamination and are generally more cemented (Fig. 10C to E). In these deposits, typical marine phreatic fabric such as high-Mg and aragonite, fibrous to bladed isopachous cements can be found (Fig. 10D and E). Fenestrae are common within 'chevrons', aeolianites, and beach/intertidal deposits.

Granulometry

Grain-size analysis was carried out on 11 beach, nine aeolianite and six 'chevron' samples from three Bahamian islands: Eleuthera, Great Exuma and Long (Supp. Data). Among the beach samples, 27% are qualified as fine sand, 27% as medium sand, 9% as coarse sand and 36% are classified in the gravelly sand textural group. For aeolian samples, 55.5% are composed of fine sand, 33% of medium sand and 11% of coarse sand. Finally, 'chevrons' consist of finer material with half of the corresponding samples being respectively fine-grained, and the other half qualifying as medium sand.

Amino-acid racemization dating

The A/I ratios calculated from D/L Glu ratios measured on the four samples collected from the studied 'chevrons' range from 0.39 to 0.48 (Table 1). These values can be assigned to the aminozone E, which has been correlated to MIS 5e by comparison with U-Th ages of stratigraphically equivalent reef terraces (Hearty & Kaufman, 2009, 2000). In particular, the age

of the samples gathered from the Farmer's Hill (Great Exuma; EFH in Figs 5A and 8E) and Miller's Settlement (Long Island; LMI in Figs 5C and 8A) sections could correspond to the first depositional phase identified in the LIG (5eI; Hearty & Kaufman, 2009, 2000), whereas that of samples from the Rokers Point Settlement section (Great Exuma; ERP in Figs 5A and 8B) and from the Old Gray's Settlement (Long Island; LOG in Figs 5D and 8E) sections could coincide with the second phase of deposition (5eII).

DISCUSSION

Depositional nature of 'chevrons'

Morphological criteria

Based on qualitative morphological observations, other authors (e.g. Engel *et al.*, 2015; Kindler & Strasser, 2002, 2000) have previously interpreted Bahamian 'chevrons' as aeolian parabolic dunes. This paper provides *quantitative* data that support this interpretation. The comparative 95 dunes (Appendix 2), despite being of different age and composition, were selected because they lie in similar coastal environments (Fig. 6), and were all characterized and defined as aeolian parabolic dunes by previous studies. If 'chevrons' were deposited by coastal aeolian processes, they are expected to share some morphological criteria, or at least to be of the same order of magnitude as the studied parabolic dunes. Indeed, following the classification of simple dunes defined by Pye (1993), and based on their L/W ratios, 'chevrons' and parabolic dunes are both described as lobate or elongated with $1.04 < L/W < 5.29$ (Fig. 11A). A linear regression modelled from the whole cluster shows a mean L/W ratio = 2.44 with a relatively high coefficient of determination ($R^2 = 0.71$). The L/H ratios (Fig. 11B) display a larger spread, but once again, 'chevrons' plot within the parabolic-dune cluster. Further, the ratio between the stoss-slope and the lee-face angles (φ/α) of 'chevrons' and parabolic dunes follows an exponential law with a good level of confidence ($R^2 = 0.61$). In other words, the stoss-slope angle exponentially increases with the lee-side angle (Fig. 11C). Further, similar to aeolian bedforms, the concave lee face of 'chevrons' is steeper than the convex stoss slope, indicating a migration by grainfall and avalanching of the material transported from or through the deflation basin. Finally, although the W/H plot (Fig. 11D) shows that 'chevrons' tend to be slightly wider than high compared to the majority of aeolian dunes, their ranges overlap.

As discussed in previous reports (Engel *et al.*, 2015; Kindler & Strasser, 2002, 2000; Mylroie, 2018a), interpreting 'chevrons' as storm-wave deposits does not agree with current present-day knowledge of the latter. Indeed, recent hurricane sediments consist of *localized* sand sheets, conglomeratic berms and washover fans or lobes (Fig. 12; Donnelly *et al.*, 2006; Donnelly & Sallenger, 2007; Mattheus & Fowler, 2015; Morton *et al.*, 2007; Williams, 2011) that are several orders of magnitude smaller than 'chevrons' (table 4 in Morton *et al.*, 2007; Jamison-Todd *et al.*, 2020) and never display such a V-shaped morphology (Engel *et al.*, 2015). Finally, sandy storm deposits are systematically thinning landward with slopes ranging from 1° to 5° whereas 'chevrons', like parabolic dunes, are thickening as they progress inland (Figs 5 and 6) with the highest elevation lying near the ridge apex (Hearty *et al.*, 1998; Hearty & Tormey, 2017; Vimpere *et al.*, 2019).

Sedimentological criteria

Hearty *et al.* (1998, 2002), Hansen *et al.* (2020, 2016), Hearty & Tormey (2017) and Tormey (1999) excluded an aeolian origin for the 'chevrons' because of the scarcity of steeply dipping foresets in these landforms. However, as emphasized by Goudie (2011), high-angle strata are relatively rare among the foreset beds of aeolian parabolic dunes. Moreover, most 'chevron' exposures are roadcuts that obliquely transect their arms and nose, thus exposing apparent dip angles of strata that are less than the true dip values. Lastly, recently discovered (Fig. 8E) and previously described outcrops of 'chevrons' (e.g. fig. 2, Hearty *et al.*, 1998) undeniably display large-scale, steeply dipping foresets. These sedimentary structures are thus more common than formerly assessed, and this occurrence reinforces the resemblance of 'chevrons' with aeolian parabolic dunes. This similarity is further supported by the presence of CTS *throughout* these deposits (Engel *et al.*, 2015; Kindler & Strasser, 2002, 2000; this paper), i.e. not only in "a few small (1`–2 m^2) patches" (Hearty *et al.*, 2015).

Furthermore, the internal architecture of the 'chevron' arms (Fig. 7) is practically identical in cross-section to that of the arms of parabolic dunes (Fig. 13). Stratification steepens from the inside part (the deflation basin) towards the outer flank where grainfall and grainflow are the main processes controlling sand movement. Low-angle, planar cross-beds prevail in the internal side of the arms (Fig. 8A and B), whereas steep foresets constitute the external side of the arm (Fig. 8C). These structures indicate a migration from the deflation basin towards the outside,

perpendicular to the main orientation of the parabolic dune (McKee, 1966; McKee & Bigarella, 1979).

Finally, comparing the internal structures of washover deposits (e.g. Schwartz, 1982) with those of 'chevrons' (Figs 12 and 14) underlines the dissimilarities between the two. Washover sediments pile up during one single and sudden event (i.e. a storm) and, consequently, do not include pedogenic features. In contrast, 'chevrons' accumulate under discontinuous aeolian processes, which leads to the formation of protosols during the sedimentation breaks. Moreover, in strike section, washover deposits display subhorizontal stratification (Fig. 14A), but lack cross-bed sets and highly inclined sets (except for washovers where the flow carried sediments into a standing body of water; Schwartz, 1982). In contrast, a complete strike section across a 'chevron' (Fig. 14B) shows the classic aeolian succession of backsets, topsets and foresets. Backsets dip seaward at medium angle whilst steep topsets dip landward, thus indicating a landward migration of the ridges (Rowe & Bristow, 2015b). To sum up, all sedimentological observations indicate an aeolian rather than a storm-wave origin for the Bahamian 'chevrons'.

Granulometric criteria

Applying the Folk and Ward method to the collected granulometric data (Appendix 5) indicates a pure (100% of sand) sandy composition for both 'chevron' and aeolian sediments, whereas coarser beach material is made up of slightly gravelly sand (98.2% of sand and 1.8% of very fine gravel; Fig. 15A). The same trend is also observable when comparing mean grain sizes which amount to 272.4 µm (1.876 ϕ) and 271.3 µm (1.882 ϕ) for 'chevrons' and aeolianites, respectively, and to 377.2 µm (1.407 ϕ) for beaches.

The sorting is somewhat better within 'chevrons' (1.593 µm; 0.671 ϕ; moderately well-sorted) and aeolianites (1.542 µm; 0.625 ϕ; moderately well-sorted) than in beach deposits (1.954 µm; 0.966 ϕ; moderately sorted). These values are to be considered carefully because the three types of deposits do not show a normal or gaussian distribution (Fig. 15B), but rather a bimodal one for 'chevrons' ($M1_{ch}$ = 196.0 µm; $M2_{ch}$ = 327.5 µm) and aeolianites ($M1_a$ = 231.0 µm; $M2_a$ = 655.0 µm), and a polymodal one for beaches ($M1_b$ = 231.0 µm; $M2_b$ = 327.5 µm; $M3_b$ = 655.0 µm).

The Lilliefors test, a derivative of the Kolmogorov–Smirnov test for cases where parameters of the normal law, mean and variance are unknown, was applied as a normality test. It systematically rejects the hypothesis that beach, aeolian and 'chevron' grain-size distribution are

normally distributed with p-values <0.0001. Taken by sample, 36% of beach sediments are unimodal, 9% bimodal, 36% trimodal and 18% polymodal (Supp. Data). Aeolianites are considerably more unimodal deposits (78%) but contain 11% of bimodal and polymodal samples. 'Chevrons' show 50% of bimodal, 33% trimodal and 17% polymodal distribution. To sum up, beach sediments tend to have a unimodal to polymodal distribution, whereas aeolian sands are unimodal and 'chevrons' are mostly bimodal.

The cumulative percentile values D_{10}, D_{50} (the median) and D_{90} are, respectively: 157.0 µm, 261.4 µm and 500.9 µm for 'chevrons'; 166.3 µm, 258.4 µm and 527.3 µm for aeolianites; and 181.2 µm, 340.4 µm and 983.6 µm for beaches. Because of the non-normal character of distributions, skewness and kurtosis values may just serve as indicators at best. However, it is worth mentioning that, despite being all coarsely skewed, the distribution is mesokurtic for 'chevrons', leptokurtic for aeolianites and platykurtic for beaches. These graphical observations were then confirmed by applying the Wilcoxon–Mann–Whitney statistical test to compare the different grain-size populations. Some approximation was used to compute the p-values, and the continuity correction has been applied. The null hypothesis H0, which considers no difference between the compared grain-size populations, was rejected when comparing beach samples with aeolian and 'chevron' sediments with p-values <0.0001. Conversely, it cannot be rejected when comparing aeolian and 'chevron' grain-size populations because of a p-value computed at 0.868.

In summary, these quantitative analyses and statistical tests demonstrate that the granulometry of 'chevrons' is akin to that of aeolianites, and that both differ from that of beaches, further suggesting deposition by wind and not by water. The studied aeolianites are mostly foredunes, which are constantly fed by a close profusive source of well-sorted sediment from the beach. Thus, they commonly display a unimodal grain-size distribution. By contrast, parabolic dunes (i.e. 'chevrons') are migrating further inland, thus moving away from coastal sources of sediment. In this case, a bimodal grain-size distribution indicates that dunes have incorporated sand from the deflation basin (Brookfield & Ahlbrandt, 2000; Pye & Tsoar, 2008).

Origin of high-elevation fenestral porosity

The 'chevrons' mostly consist of an alternation of decimetre-thick, finely laminated (CTS) beds and of non-laminated or poorly laminated intervals of equal thickness comprising numerous fenestrae (Fig. 9A), which can be observed at elevations exceeding 30 m. As stated above, one school of thought (e.g. Hearty *et al.*, 2002, 1998; Hearty & Tormey, 2017; Wanless *et al.*, 1989) suggests that fenestral porosity formed by large-wave action, concurrent with the deposition of 'chevrons', and that aeolian structures were produced on the surface of these deposits during periods of relative quiescence between 'superstorms'. The other group (e.g. Kindler & Strasser, 2002, 2000; Mylroie, 2018a, 2018b) proposed that fenestrae were generated by heavy rainfall on the previously wind-deposited 'chevrons'. The present authors believe that both hypotheses are improbable. To begin with, the formation of fenestral porosity by swash action up to 30 m should have been accompanied by erosion of the dune topography and/or by input of coarse-grained (possibly shelly) material, which is never the case. Secondly, although the creation of rain-induced fenestrae has been observed in modern dunes (Emery, 1945), it is a rare phenomenon that cannot account for such extensive features. Further, the presence of such fenestrae in fossil aeolianites (e.g. Bain & Kindler, 1994) is speculative because they have never been observed in association with more typical features such as raindrop imprints.

It has long been known that fenestrae are polygenetic features that are not necessarily generated by swash action in the intertidal zone (Kindler, 1991; Shinn, 1983, 1968). They can be related to the decay of organic matter such as plant roots and/or microbial mats, which are common in aeolian sediments. Relying on the observation of fungal endoliths and sparmicritized zones associated with elevated fenestrae in a Pleistocene aeolianite from Providenciales (Caicos Platform), Kindler *et al.* (2009) further proposed that fenestral zones represented immature pedogenic horizons where the cemented grainstone was patchily altered by plant and fungal activity. The authors tend to support this hypothesis because of the unequivocal association of parabolic dunes with a stabilizing vegetation (e.g. Durán & Herrmann, 2006; Durán & Moore, 2013; Tsoar & Blumberg, 2002; Yan & Baas, 2015). Furthermore, the higher density of fenestral beds in 'chevron' arms, with respect to the apices, can be explained by the formation process of parabolic dunes implying a fixation of the trailing arms by vegetation while bare sand composes the migrating nose (e.g. Goudie, 2011).

With one exception (Blackwatch Pass, Bermuda; Kindler & Strasser, 2000; Rowe & Bristow, 2015a, 2015b), elevated fenestrae have always been observed in well-sorted oolitic-peloidal grainstone and in association with CTS (Fig. 10B; figs 6 and 7 in Hearty *et al.*, 1998; fig. 3 in Kindler & Strasser, 2002). Thus, the occurrence of such pores could also result from the interaction of vadose water (but not necessarily heavy rainfall) with the peculiar grain shape and size of the oolites, and with the tight packing and low permeability of the CTS.

Megaboulders of Eleuthera

As previously stated, Hearty *et al.* (1998, 2002) and Hearty & Tormey (2018a, 2017) repeatedly argued that a 'trilogy' of sedimentary features, including the 'chevrons', 'runup' deposits and the megaboulders from North Eleuthera, offered an unequivocal testimony of superstorms producing giant, long-period waves in the north-east Atlantic Ocean at the end of the LIG.

Based on new quantitative data, the present study substantiates earlier reports (e.g. Kindler & Strasser, 2000) according to which the 'chevrons' must be interpreted as aeolian parabolic dunes. Because they also display numerous aeolian structures (for example, CTS), this study further supports the interpretation of 'run-up' deposits as climbing (Kindler & Strasser, 2000) or advancing (Rowe & Bristow, 2015b) dunes. It is beyond the scope of this paper to discuss the age of emplacement of the megaboulders, and whether they represent the remnants of a tower karst (Mylroie, 2018a, 2008), were rolled down from a higher elevation, or deposited by large waves related to bank-margin collapse (Hearty, 1997), a tsunami (Hearty, 1997; Kelletat *et al.*, 2004), a superstorm (Hearty *et al.*, 1998; Hearty & Tormey, 2018b, 2017), or a hurricane of historical intensity during a period of higher than present sea level (Rovere *et al.*, 2018, 2017). However, the authors assert that the aforementioned deposits must not be regrouped in a 'trilogy' because 'chevrons' and 'run up' deposits are considered to be the result of long-term aeolian transport on several islands, whereas the megaboulders from North Eleuthera have likely been emplaced by a violent, short-term event at one location.

Age of 'chevrons'

Based on AAR data from this and the Hearty *et al.* (1998) studies, the Bahamian 'chevrons' can be assigned to MIS 5e, but the AAR-dating method is not precise enough to unequivocally correlate

these deposits with a specific interval of this substage. Considering their morphological position (Hearty *et al.*, 1998) and the occurrence of cross-beds dipping below modern sea level (Kindler & Strasser, 2002), previous authors have suggested that 'chevron' deposition occurred during the rapid regression that ensued MIS 5e, when large amounts of mostly oolitic shelf sediments became available for reworking by wind or waves (Hearty *et al.*, 2015; Kindler & Strasser, 2000; Neumann & Hearty, 1996). This timing and scenario are likely correct for the low-elevation 'chevrons' located near platform margins (for example, Harvey Cays, Exumas; fig. 2 in Hearty *et al.*, 1998), but questionable when applied to the higher ridges positioned in a more bankward position (for example, the landforms on Great Exumas, Fig. 5A and B). The latter were probably emplaced during or before the previous LIG highstand (interval 5 of Hearty & Tormey, 2017; Hearty *et al.*, 2007) *ca* 118 ka BP (Kerans *et al.*, 2019; Skrivanek *et al.*, 2018).

Palaeoclimatic and palaeoceanographic settings during the formation of 'chevrons'

Kindler & Strasser (2000) have already addressed the question of the climatic and oceanographic conditions on GBB during the formation of 'chevrons'. To sum up, the environment was potentially windier and certainly drier than today to prevent the rapid cementation of carbonate sands (e.g. Kindler & Mazzolini, 2001) that would hinder dune migration. That climatic conditions were drier during the formation of 'chevrons' and of coeval linear dunes is attested to by the occurrence of nebkhas within these deposits (Kindler & Strasser, 2000; Tormey, 1999). Indeed, nebkhas, or 'coppice dunes', characterize areas of low precipitation ranging from 200 to 300 mm/yr (García-Romero *et al.*, 2019). In comparison, today's annual rainfall across the Bahamas varies between 600 mm and 1500 mm (Wolcott *et al.*, 2018). Lower precipitation rates likely induced a change in both vegetation type and cover, which directly impacts the roughness of the terrain (e.g. Jerolmack *et al.*, 2012; Levin *et al.*, 2008), and thus on how the wind is slowed down during its progression inland. Drier climatic conditions generally result in shrubbier vegetation at these latitudes, representing a lower surface roughness (De Chiffre, 2001), which increases the wind capacity to transport sediment (drift potential; Fryberger & Dean, 1979) without necessarily blowing harder. Such a setting could have resulted from a slight northward migration of climatic belts (Perlmutter & Matthews, 1992) placing GBB in the same conditions as those presently affecting the southern Bahamas. These speculations are supported by recent climate models

advocating for a higher surface temperature, diminished precipitation and a grassier type of vegetation during a great part of the MIS 5e (Nikolova *et al.*, 2013; Scussolini *et al.*, 2019).

Furthermore, considering the reconstruction of the Bahamian climate during MIS 5e proposed by Zhuravleva & Bauch (2018), the following scenario can be envisaged. An important phase of carbonate (i.e. ooid) production occurred early in MIS 5e, when warm and humid conditions associated with weak trade winds prevailed. The elevated 'chevrons', that have migrated further inland, could correspond to a sedimentation phase taking place during the 'Younger Dryas-like event' (*ca* 127 ka BP) when climate was drier and windier due to a sudden southward motion of the ITCZ. Deposition of the low-elevation 'chevrons' followed a second phase of carbonate production, and likely occurred during the stepwise regression that ensued the second (or the main) MIS 5e highstand (Fig. 2), when the ITCZ shifted again to the south.

Thus, a protracted influence of trade winds, a lowering of the moisture content in the sediment, and both a vegetation cover and type subsequently dropping within the ideal range for parabolic dune formation (Goudie, 2011, for a summary; Hanoch *et al.*, 2018) would have favoured the deposition of these ridges by increasing the erosional power of wind on loose foredunes, forming blowout features of different stages (e.g. Hesp, 2011). The wind would have reworked these foredunes and the fine part of the beach material (explaining the matching of some grain-size populations within the ridges; Fig. 15), sorting out the latter during the migration processes. These conditions would have lasted until after the onset of the regression (as shown by the foresets dipping below modern datum), when the shelf sediments became exposed, spanning the whole highstand in agreement with the recent models proposed for carbonate aeolianites (Frébourg, 2010; Rowe & Bristow, 2015a).

CONCLUSIONS

The new morphological, granulometric, sedimentological and age data on Bahamian 'chevrons' presented in this study, as well as a detailed review of previous papers pertaining to these peculiar landforms bring out the following conclusions:

- The morphological parameters measured on the 'chevrons' from Great Exuma, Long and Acklins islands perfectly correlate with those of more than 95 aeolian parabolic dunes worldwide.

- The occurrence of numerous aeolian structures in these deposits, along with strong dissimilarities with storm-related deposits, confirm that 'chevrons' are wind-deposited bedforms.
- Quantitative granulometric analyses and several statistical tests show that the granulometry of 'chevrons' is akin to that of aeolianites, but differs from that of beaches, further suggesting that they have been deposited by wind and not by water.
- Considering the polygenetic nature of fenestral porosity and the unequivocal relationship between vegetation and parabolic dunes, it is reasonable to assume that high-elevation fenestrae are related to plant or fungal activity, and/or to the particular fabric of the well-sorted oolitic–peloidal aeolianites.
- Amino-acid racemization (AAR) data constrain the 'chevron' age to Marine Isotope Stage (MIS) 5e, and geomorphological criteria further indicate they have probably been formed during two distinct late phases of this time interval.
- The notorious 'chevrons' from Eleuthera Island are linear ridges.

In summary, the peculiar and controversial Bahamian 'chevrons' are aeolian parabolic dunes that have been deposited during the MIS 5e highstand and the ensuing regression, when climatic conditions in the northern Bahamas were drier and windier than today due to a southward displacement of the average annual position of the Intertropical Convergence Zone (ITCZ). These conditions were coupled with shrubbier/grassier vegetation, inducing the formation of fenestral porosity, and fixing the trailing arms while a migrating nose was advancing downwind farther inland.

ACKNOWLEDGEMENTS

This project was funded by the Department of Earth Sciences of the University of Geneva. Our gratitude goes to the Earth Observation Centre at the German Aerospace Centre (DLR) for generously providing the DEMs needed. Dr Ian Spooner at Acadia University helped this project by allowing us to use his drone in the field. We would like to acknowledge the Amino Acid Geochronology Lab. of the Northern Arizona University for their efficiency and for remaining available to discuss the results. We thank François Gischig for the excellent quality of the thin sections. Comments of André Strasser, Ryan C. Ewing and Massimiliano Ghinassi greatly improved the paper. The authors declare no conflict of interest associated with this publication.

DATA AVAILABILITY STATEMENT

The data that support the findings of this study are available from the corresponding author upon reasonable request.

REFERENCES

Bain, R., Kindler, P., 1994. Irregular fenestrae in Bahamian eolianites: a rainstorm-induced origin. J. Sediment. Res. 64.

Barlow, N.L.M., McClymont, E.L., Whitehouse, P.L., Stokes, C.R., Jamieson, S.S.R., Woodroffe, S.A., Bentley, M.J., Callard, S.L., Cofaigh, C.Ó., Evans, D.J.A., Horrocks, J.R., Lloyd, J.M., Long, A.J., Margold, M., Roberts, D.H., Sanchez-Montes, M.L., 2018. Lack of evidence for a substantial sea-level fluctuation within the Last Interglacial. Nat. Geosci. 11, 627–634. https://doi.org/10.1038/s41561-018-0195-4

Blott, S.J., Pye, K., 2001. GRADISTAT: a grain size distribution and statistics package for the analysis of unconsolidated sediments. Earth Surf. Process. Landf. 26, 1237–1248. https://doi.org/10.1002/esp.261

Bourgeois, J., Weiss, R., 2009. "Chevrons" are not mega-tsunami deposits - A sedimentologic assessment. Geology 37, 403–406. https://doi.org/10.1130/G25246A.1

Brookfield, M.E., Ahlbrandt, T.S., 2000. Eolian sediments and processes. Elsevier.

Caputo, M.V., 1995. Sedimentary architecture of Pleistocene eolian calcarenites, San Salvador Island, Bahamas, in: Terrestrial and Shallow Marine Geology of the Bahamas and Bermuda. Geological Society of America. https://doi.org/10.1130/0-8137-2300-0.63

Caputo, M.V., 1993. Eolian Structures and Textures in Oolitic- Skeletal Calcarenites from the Quaternary of San Salvador Island, Bahamas: A New Perspective on Eolian Limestones, in: Mississippian Oolites and Modern Analogs, Studies in Geology. American Association of Petroleum Geologists, pp. 243–259.

Carew, J., Mylroie, J., 2001. Quaternary carbonate eolianites of the Bahamas: useful analogues for the interpretation of ancient rocks?, in: Modern and Ancient Carbonate Eolianites: Sedimentology, Sequence Stratigraphy, and Diagenesis, SEPM Special Publication. pp. 33–45.

Carew, J., Mylroie, J., 1995a. Quaternary tectonic stability of the Bahamian Archipelago: Evidence from fossil coral reefs and flank margin caves. Quat. Sci. Rev. 14, 145–153.

Carew, J., Mylroie, J., 1995b. Depositional model and stratigraphy for the Quaternary geology of the Bahama Islands, in: Terrestrial and Shallow Marine Geology of the Bahamas and Bermuda. Geological Society of America. https://doi.org/10.1130/0-8137-2300-0.5

Carew, J., Mylroie, J., 1985. Pleistocene and Holocene stratigraphy of San Salvador Island, Bahamas, with reference to marine and terrestrial lithofacies at French Bay, in: Curran, H. (Ed.), Orlando Annual Meeting Field Trip Guidebook, Geological Society of America. Bahamian Field Station, San Salvador Island Bahamas, pp. 11–61.

Chen, J., Curran, H., White, B., Wasserburg, G., 1991. Precise chronology of the last interglacial period: 234U-230Th data from fossil coral reefs in the Bahamas. Geol. Soc. Am. Bull. 103, 82–97.

De Chiffre, L., 2001. Measurement of surface roughness. DTU, Institut for Produktion og Ledelse.

DeConto, R., Pollard, D., 2016. Contribution of Antarctica to past and future sea-level rise. Nature 531, 591–597. https://doi.org/10.1038/nature17145

Donnelly, C., Kraus, N., Larson, M., 2006. State of Knowledge on Measurement and Modeling of Coastal Overwash. J. Coast. Res. 224, 965–991. https://doi.org/10.2112/04-0431.1

Donnelly, C., Sallenger, A.H., 2007. Characterisation and Modeling of Washover Fans, in: Coastal Sediments '07. Presented at the Sixth International Symposium on Coastal Engineering and Science of Coastal Sediment Process, American Society of Civil Engineers, New Orleans, Louisiana, United States, pp. 2061–2073. https://doi.org/10.1061/40926(239)162

Donovan, B., Tormey, B., 2015. What's past is prologue: Evidence of climate instability and intense storms during the Last Interglacial on Eleuthera Island, Bahamas., in: GSA Abstracts with Programs. Presented at the GSA Southeastern Section - 64th Annual Meeting, Chattanooga, p. 75.

Dunham, R., 1970. Keystone vugs in carbonate beach deposits. AAPG Bull. 54, 845.

Durán, O., Herrmann, H., 2006. Vegetation Against Dune Mobility. Phys. Rev. Lett. 97. https://doi.org/10.1103/PhysRevLett.97.188001

Durán, O., Moore, L., 2013. Vegetation controls on the maximum size of coastal dunes. Proc. Natl. Acad. Sci. 110, 17217–17222.

Dutton, A., Carlson, A.E., Long, A.J., Milne, G.A., Clark, P.U., DeConto, R., Horton, B.P., Rahmstorf, S., Raymo, M.E., 2015. Sea-level rise due to polar ice-sheet mass loss during past warm periods. Science 349, aaa4019–aaa4019. https://doi.org/10.1126/science.aaa4019

Emery, K., 1945. Entrapment of air in beach sand. J. Sediment. Res. 15.

Engel, M., Kindler, P., Godefroid, F., 2015. Speculations on superstorms–Interactive comment on" Ice melt, sea level rise and superstorms: evidence from paleoclimate data, climate modeling, and modern observations that 2° C global warming is highly dangerous" by J. Hansen *et al.* Atmospheric Chem. Phys. Discuss. 15, C6270–C6281.

Folk, R., Ward, W., 1957. Brazos River bar [Texas]; a study in the significance of grain size parameters. J. Sediment. Res. 27, 3–26.

Frébourg, G., 2010. Carbonate coastal dunes: potential reservoir rocks? University of Geneva.

Frébourg, G., Hasler, C.-A., Le Guern, P., Davaud, E., 2008. Facies characteristics and diversity in carbonate eolianites. Facies 54, 175–191. https://doi.org/10.1007/s10347-008-0134-8

Friedman, G., Johnson, K., 1982. Exercises in sedimentology. John Wiley & Sons.

Friedman, G., Sanders, J., 1978. Principles of sedimentology. Wiley.

Fryberger, S., Dean, G., 1979. Dune forms and wind regime, in: A Study of Global Sand Seas. US Government Printing Office Washington, pp. 137–169.

Fryberger, S., Schenk, C., 1988. Pin stripe lamination: a distinctive feature of modern and ancient eolian sediments. Sediment. Geol. 55, 1–15.

García-Romero, L., Hesp, P.A., Peña-Alonso, C., Miot da Silva, G., Hernández-Calvento, L., 2019. Climate as a control on foredune mode in Southern Australia. Sci. Total Environ. 694, 133768. https://doi.org/10.1016/j.scitotenv.2019.133768

Gibson, K.A., Peterson, L.C., 2014. A 0.6 million year record of millennial-scale climate variability in the tropics: GIBSON AND PETERSON; TROPICAL MILLENNIAL-SCALE CLIMATE CHANGE. Geophys. Res. Lett. 41, 969–975. https://doi.org/10.1002/2013GL058846

Godefroid, F., 2012. Géologie de Mayaguana, SE de l'archipel des Bahamas. University of Geneva, Geneva.

Goudie, A., 2011. Parabolic Dunes: Distribution, Form, Morphology and Change 7.

Hanoch, G., Yizhaq, H., Ashkenazy, Y., 2018. Modeling the bistability of barchan and parabolic dunes. Aeolian Res. 35, 9–18. https://doi.org/10.1016/j.aeolia.2018.07.003

Hansen, J., Kharecha, P., Sato, M., Masson-Delmotte, V., Ackerman, F., Beerling, D., Hearty, P., Hoegh-Guldberg, O., Hsu, S.-L., Parmesan, C., Rockstrom, J., Rohling, E., Sachs, J., Smith, P., Steffen, K., Van Susteren, L., von Schuckmann, K., Zachos, J., 2013. Assessing "Dangerous Climate Change": Required Reduction of Carbon Emissions to Protect Young

People, Future Generations and Nature. PLoS ONE 8, e81648. https://doi.org/10.1371/journal.pone.0081648

Hansen, J., Sato, M., Hearty, P., Ruedy, R., Kelley, M., Masson-Delmotte, V., Russell, G., Tselioudis, G., Cao, J., Rignot, E., Velicogna, I., Tormey, B., Donovan, B., Kandiano, E., von Schuckmann, K., Kharecha, P., Legrande, A.N., Bauer, M., Lo, K.-W., 2020. Ice Melt, Sea Level Rise and Superstorms: Evidence from Paleoclimate Data, Climate Modeling, and Modern Observations Implies that 2°C Global Warming Above the Preindustrial Level Would Be Dangerous, in: Earth and Its Atmosphere. Vide Leaf, Hyderabad. https://doi.org/10.37247/EA.1.2020.13

Hansen, J., Sato, M., Hearty, P., Ruedy, R., Kelley, M., Masson-Delmotte, V., Russell, G., Tselioudis, G., Cao, J., Rignot, E., Velicogna, I., Tormey, B., Donovan, B., Kandiano, E., von Schuckmann, K., Kharecha, P., Legrande, A.N., Bauer, M., Lo, K.-W., 2016. Ice melt, sea level rise and superstorms: evidence from paleoclimate data, climate modeling, and modern observations that 2 °C global warming could be dangerous. Atmospheric Chem. Phys. 16, 3761–3812. https://doi.org/10.5194/acp-16-3761-2016

Hasler, C.-A., Simpson, G., Kindler, P., 2010. Platform margin collapse simulation: The case of the North Eleuthera massive boulders, in: Abstracts and Program. Presented at the 15th Symposium on the Geology of the Bahamas and Other Carbonate Regions, San Salvador Island, Bahamas, Gerace Research Center, pp. 22–23.

Hearty, P., 2010. Chronostratigraphy and morphological changes in Cerion land snail shells over the past 130ka on Long Island, Bahamas. Quat. Geochronol. 5, 50–64. https://doi.org/10.1016/j.quageo.2009.09.005

Hearty, P., 1997. Boulder Deposits from Large Waves during the Last Interglaciation on North Eleuthera Island, Bahamas. Quat. Res. 48, 326–338. https://doi.org/10.1006/qres.1997.1926

Hearty, P., Kaufman, D., 2009. A Cerion-based chronostratigraphy and age model from the central Bahama Islands: Amino acid racemization and 14C in land snails and sediments. Quat. Geochronol. 4, 148–159. https://doi.org/10.1016/j.quageo.2008.08.002

Hearty, P., Kaufman, D., 2000. Whole-Rock Aminostratigraphy and Quaternary Sea-Level History of the Bahamas. Quat. Res. 54, 163–173. https://doi.org/10.1006/qres.2000.2164

Hearty, P., Kindler, P., 1993. New perspectives on Bahamian geology: San Salvador Island, Bahamas. J. Coast. Res. 577–594.

Hearty, P., Neumann, A., Kaufman, D., 1998. Chevron ridges and runup deposits in the Bahamas from storms late in oxygen-isotope substage 5e. Quat. Res. 50, 309–322.

Hearty, P., Schellenberg, S., 2008. Integrated Late Quaternary chronostratigraphy for San Salvador Island, Bahamas: Patterns and trends of morphological change in the land snail Cerion. Palaeogeogr. Palaeoclimatol. Palaeoecol. 267, 41–58. https://doi.org/10.1016/j.palaeo.2008.06.003

Hearty, P., Tormey, B., 2018a. Discussion of: Mylroie, JE, 2018. Superstorms: Comments on Bahamian Fenestrae and Boulder Evidence from the Last Interglacial. Journal of Coastal Research, 34 (6), 1471–1483. J. Coast. Res. 34, 1503–1511. https://doi.org/10.2112/JCOASTRES-D-18A-00003.1

Hearty, P., Tormey, B., 2018b. Listen to the whisper of the rocks, telling their ancient story. Proc. Natl. Acad. Sci. 115, E2902–E2903. https://doi.org/10.1073/pnas.1721253115

Hearty, P., Tormey, B., 2017. Sea-level change and superstorms; geologic evidence from the last interglacial (MIS 5e) in the Bahamas and Bermuda offers ominous prospects for a warming Earth. Mar. Geol. 390, 347–365. https://doi.org/10.1016/j.margeo.2017.05.009

Hearty, P., Tormey, B., Donovan, B., Tselioudis, G., 2015. Reply to Engel, Kindler, and Godefroid's comment on "Ice melt, sea level rise and superstorms: evidence from paleoclimate data, climate modeling, and modern observations that 2°C global warming is highly dangerous" by J. Hansen *et al.*

Hearty, P., Tormey, B., Neumann, A., 2002. Discussion of "Palaeoclimatic significance of co-occurring wind-and water-induced sedimentary structures in the last-interglacial coastal deposits from Bermuda and the Bahamas"(Kindler and Strasser, 2000, Sedimentary Geology, 131, 1–7). Sediment. Geol. 147, 429–435.

Hearty, P.J., Hollin, J.T., Neumann, A.C., O'Leary, M.J., McCulloch, M., 2007. Global sea-level fluctuations during the Last Interglaciation (MIS 5e). Quat. Sci. Rev. 26, 2090–2112. https://doi.org/10.1016/j.quascirev.2007.06.019

Hearty, P.J., Neumann, A.C., 2001. Rapid sea level and climate change at the close of the Last Interglaciation (MIS 5e): evidence from the Bahama Islands. Quat. Sci. Rev. 20, 1881–1895. https://doi.org/10.1016/S0277-3791(01)00021-X

Hesp, P., 2011. Dune Coasts, in: Wolanski, E., McLusky, D. (Eds.), Treatise on Estuarine and Coastal Science. Elsevier, pp. 193–221. https://doi.org/10.1016/B978-0-12-374711-2.00310-7

Higgins, M.D., 2000. Measurement of crystal size distributions. Am. Mineral. 85, 1105–1116. https://doi.org/10.2138/am-2000-8-901

Hoffman, J.S., Clark, P.U., Parnell, A.C., He, F., 2017. Regional and global sea-surface temperatures during the last interglaciation. Science 355, 276–279. https://doi.org/10.1126/science.aai8464

Hollin, J., 1965. Wilson's Theory of Ice Ages. Nature 208, 12–16. https://doi.org/10.1038/208012a0

Hollin, J., Smith, F., Renouf, J., Jenkins, D., 1993. Sea-cave temperature measurements and amino acid geochronology of British Late Pleistocene Sea stands. J. Quat. Sci. 8, 359–364. https://doi.org/10.1002/jqs.3390080407

Hunter, R., 1977. Basic types of stratification in small eolian dunes. Sedimentology 24, 361–387.

Jamison-Todd, S., Stein, N., Overeem, I., Khalid, A., Trower, E.J., 2020. Hurricane Deposits on Carbonate Platforms: A Case Study of Hurricane Irma Deposits on Little Ambergris Cay, Turks and Caicos Islands. J. Geophys. Res. Earth Surf. 125. https://doi.org/10.1029/2020JF005597

Jerolmack, D.J., Ewing, R.C., Falcini, F., Martin, R.L., Masteller, C., Phillips, C., Reitz, M.D., Buynevich, I., 2012. Internal boundary layer model for the evolution of desert dune fields. Nat. Geosci. 5, 206–209. https://doi.org/10.1038/ngeo1381

Kaufman, D., Manley, W., 1998. A new procedure for determining DL amino acid ratios in fossils using reverse phase liquid chromatography. Quat. Sci. Rev. 17, 987–1000.

Kelletat, D., Scheffers, A., Scheffers, S., 2004. Holocene tsunami deposits on the Bahaman Islands of Long Island and Eleuthera. Z. Für Geomorphol. 48, 519–540.

Kerans, C., Zahm, C., Bachtel, S., Hearty, P., Cheng, H., 2019. Anatomy of a late Quaternary carbonate island: Constraints on timing and magnitude of sea-level fluctuations, West

Caicos, Turks and Caicos Islands, BWI. Quat. Sci. Rev. 205, 193–223. https://doi.org/10.1016/j.quascirev.2018.12.010

Kindler, P., 1991. Keystone vugs in coastal dunes: an example from the Pleistocene of Eleuthera, Bahamas. Presented at the Proceedings of the fifth symposium on the geology of the Bahamas., Bahamian Field Station, San Salvador, Bahamas, pp. 117–123.

Kindler, P., Godefroid, F., Chiaradia, M., Ehlert, C., Eisenhauer, A., Frank, M., Hasler, C.-A., Samankassou, E., 2011. Discovery of Miocene to early Pleistocene deposits on Mayaguana, Bahamas: Evidence for recent active tectonism on the North American margin. Geology 39, 523–526.

Kindler, P., Godefroid, F., Hasler, C.-A., Samankassou, E., 2009. Fenestral porosity in carbonate eolianites: a biological origin? New evidence from the Pleistocene of Providenciales Island (Caicos Platform), in: Pascucci, V., Andreucci, S. (Eds.), Abstract Book of the 27th IAS Meeting of Sedimentology, Alghero, Italy. p. 231.

Kindler, P., Hearty, P., 1996. Carbonate petrography as an indicator of climate and sea-level changes: new data from Bahamian Quaternary units. Sedimentology 43, 381–399. https://doi.org/10.1046/j.1365-3091.1996.d01-11.x

Kindler, P., Mazzolini, D., 2001. Sedimentology and petrography of dredged carbonate sands from Stocking Island (Bahamas). Implications for meteoric diagenesis and aeolianite formation. Palaeogeogr. Palaeoclimatol. Palaeoecol. 175, 369–379. https://doi.org/10.1016/S0031-0182(01)00380-7

Kindler, P., Mylroie, J., Curran, H., Carew, J., Gamble, D., Rothfus, T., Savarese, M., Sealey, N., 2010. Geology of Central Eleuthera, Bahamas: a field trip guide.

Kindler, P., Strasser, A., 2002. Palaeoclimatic significance of co-occurring wind- and water-induced sedimentary structures in last-interglacial coastal deposits from Bermuda and the Bahamas: response to Hearty *et al.*'s comment. Sediment. Geol. 147, 437–443. https://doi.org/10.1016/S0037-0738(01)00099-9

Kindler, P., Strasser, A., 2000. Palaeoclimatic significance of co-occurring wind-and water-induced sedimentary structures in the last-interglacial coastal deposits from Bermuda and the Bahamas. Sediment. Geol. 131, 1–7.

Kottek, M., Grieser, J., Beck, C., Rudolf, B., Rubel, F., 2006. World Map of the Köppen-Geiger climate classification updated. Meteorol. Z. 15, 259–263. https://doi.org/10.1127/0941-2948/2006/0130

Krumbein, W., Pettijohn, F., 1938. Manual of sedimentary petrography, Appleton Century. ed. Appleton Century, London.

Levin, N., Ben-Dor, E., Kidron, G., Yaakov, Y., 2008. Estimation of surface roughness (z_0) over a stabilizing coastal dune field based on vegetation and topography. Earth Surf. Process. Landf. 33, 1520–1541. https://doi.org/10.1002/esp.1621

Loope, D., Abegg, F., 2001. Recognition and geologic preservation of ancient carbonate eolianites., in: Modern and Ancient Carbonate Eolianites, SEPM Special Publication. SEPM (Society for Sedimentary Geology). https://doi.org/10.2110/pec.01.71

Loucks, R., Patty, K., 2017. Vadose Diagenetic Dissolution Textures, Cementation Patterns, and Aragonite and Mg-Calcite Alteration in the Holocene Isla Cancún Eolianite Aragonitic Ooids: Modern Analog for Ancient Ooid-Grainstone Pore Networks. Gulf Coast Assoc. Geol. Soc. J. 6, 1–20.

Loucks, R., Ward, W., 2001. Eolian stratification and beach-to-dune transition in a Holocene carbonate eolianite complex, Isla Cancun, Quintana Roo, Mexico., in: Modern and Ancient Carbonate Eolianites, SEPM Special Publication. SEPM (Society of Sedimentary Geology).

Lynts, G., 1970. Conceptual model of the Bahamian Platform for the last 135 million years. Nature 225, 1226.

Masson-Delmotte, V., Schulz, M., Abe-Ouchi, A., Beer, J., Ganopolski, A., Fidel, J., Rouco, G., Jansen, E., Lambeck, K., Luterbacher, J., Naish, T., Ramesh, R., Rojas, M., Shao, X., Anchukaitis, K., Arblaster, J., Bartlein, P.J., Benito, G., Clark, P., Comiso, J.C., Crowley, T., Deckker, P.D., de Vernal, A., Delmonte, B., DiNezio, P., Dowsett, H.J., Edwards, R.L., Fischer, H., Fleitmann, D., Foster, G., Fröhlich, C., Hall, A., Hargreaves, J., Haywood, A., Hollis, C., Krinner, G., Landais, A., Li, C., Lunt, D., Mahowald, N., McGregor, S., Meehl, G., Mitrovica, J.X., Moberg, A., Mudelsee, M., Muhs, D.R., Mulitza, S., Müller, S., Overland, J., Parrenin, F., Pearson, P., Robock, A., Rohling, E., Salzmann, U., Savarino, J., Sedláček, J., Shindell, D., Smerdon, J., Solomina, O., Tarasov, P., Vinther, B., Waelbroeck, C., Wolf,

D., Yokoyama, Y., Yoshimori, M., Zachos, J., Zwartz, D., Gupta, A.K., Rahimzadeh, F., Raynaud, D., Wanner, H., 2013. Information from Paleoclimate Archives, in: Stocker, T.F., Qin, D., Plattner, M., Tignor, A., Boschung, J., Nauels, A., Xia, Y., Bex, V., Midgley, P. (Eds.), Climate Change 2013: The Physical Science Basis. Contribution of Working Group I to the Fifth Assessment Report of the Intergovernmental Panel on Climate Change. Cambridge, p. 82.

Mattheus, C., Fowler, J., 2015. Paleotempestite Distribution across an Isolated Carbonate Platform, San Salvador Island, Bahamas. J. Coast. Res. 314, 842–858. https://doi.org/10.2112/JCOASTRES-D-14-00077.1

McKee, E., 1966. Structures of dunes at White Sands National Monument, New Mexico (and a comparison with structures of dunes from other selected areas). Sedimentology 7, 3–69. https://doi.org/10.1111/j.1365-3091.1966.tb01579.x

McKee, E., Ward, W., 1983. Eolian Environment: Chapter 3, in: M 33: Carbonate Depositional Environments. pp. 131–170.

Mckee, E.D., Bigarella, J.J., 1972. Deformational Structures in Brazilian Coastal Dunes. J. Sediment. Petrol. 42, 670–681.

Mercer, J., 1978. West Antarctic ice sheet and CO2 greenhouse effect: a threat of disaster. Nature 271, 321.

Miller, G., Brigham-Grette, J., 1989. Amino acid geochronology: resolution and precision in carbonate fossils. Quat. Int. 1, 111–128.

Morton, R.A., Gelfenbaum, G., Jaffe, B.E., 2007. Physical criteria for distinguishing sandy tsunami and storm deposits using modern examples. Sediment. Geol. 200, 184–207. https://doi.org/10.1016/j.sedgeo.2007.01.003

Mulder, T., Ducassou, E., Gillet, H., Hanquiez, V., Tournadour, E., Combes, J., Eberli, G.P., Kindler, P., Gonthier, E., Conesa, G., Robin, C., Sianipar, R., Reijmer, J.J.G., François, A., 2012. Canyon morphology on a modern carbonate slope of the Bahamas: Evidence of regional tectonic tilting. Geology 40, 771–774. https://doi.org/10.1130/G33327.1

Mullins, H., Lynts, G., 1977. Origin of the northwestern Bahama Platform: Review and reinterpretation. Geol. Soc. Am. Bull. 88, 1447–1461.

Mylroie, J., 2018a. Superstorms: Comments on Bahamian fenestrae and boulder evidence from the last interglacial. J. Coast. Res. 34, 1471–1483. https://doi.org/10.2112/JCOASTRES-D-17-00215.1

Mylroie, J., 2018b. Reply to: Hearty, P.J. and Tormey, B.R., 2018. Discussion of: Mylroie, J.E., 2018. Superstorms: Comments on Bahamian Fenestrae and Boulder Evidence from the Last Interglacial. *Journal of Coastal Research,* 34(6), 1471–1483. J. Coast. Res. 346, 1512–1515. https://doi.org/10.2112/JCOASTRES-D-18A-00004

Mylroie, J.E., 2008. Late Quaternary sea-level position: Evidence from Bahamian carbonate deposition and dissolution cycles. Quat. Int. 183, 61–75. https://doi.org/10.1016/j.quaint.2007.06.030

Neilson, M., Brockman, G., 1977. The error associated with point-counting. Am. Mineral. 62, 1238–1244.

Neumann, A., Hearty, P., 1996. Rapid sea-level changes at the close of the last interglacial (substage 5e) recorded in Bahamian island geology. Geology 24, 775–778.

Nikolova, I., Yin, Q., Berger, A., Singh, U.K., Karami, M.P., 2013. The last interglacial (Eemian) climate simulated by LOVECLIM and CCSM3. Clim. Past 9, 1789–1806. https://doi.org/10.5194/cp-9-1789-2013

Past Interglacials Working Group of PAGES, 2016. Interglacials of the last 800,000 years. Rev. Geophys. 54, 162–219. https://doi.org/10.1002/2015RG000482

Peel, M., Finlayson, B., McMahon, T., 2007. Updated world map of the Ko¨ppen-Geiger climate classification. Hydrol Earth Syst Sci 12.

Perlmutter, M., Matthews, M., 1992. Global cyclostratigraphy., University of Chicago. ed. Argonne National Laboratory.

Peterson, L.C., Haug, G.H., 2006. Variability in the mean latitude of the Atlantic Intertropical Convergence Zone as recorded by riverine input of sediments to the Cariaco Basin (Venezuela). Palaeogeogr. Palaeoclimatol. Palaeoecol. 234, 97–113. https://doi.org/10.1016/j.palaeo.2005.10.021

Pye, K., 1993. Late Quaternary Development of Coastal Parabolic Megadune Complexes in Northeastern Australia, in: Pye, K., Lancaster, N. (Eds.), Aeolian Sediments. Blackwell Publishing Ltd., Oxford, UK, pp. 23–44. https://doi.org/10.1002/9781444303971.ch3

Pye, K., Tsoar, H., 2008. Aeolian sand and sand dunes, Springer Science & Business Media.

Roduit, N., 2007. JMicroVision: un logiciel d'analyse d'images pétrographiques polyvalent. University of Geneva.

Rovere, A., Casella, E., Harris, D., Lorscheid, T., Nandasena, N., Dyer, B., Sandstrom, M., Stocchi, P., D'Andrea, W., Raymo, M., 2018. Reply to Hearty and Tormey: Use the scientific method to test geologic hypotheses, because rocks do not whisper. Proc. Natl. Acad. Sci. 115, E2904–E2905. https://doi.org/10.1073/pnas.1800534115

Rovere, A., Casella, E., Harris, D., Lorscheid, T., Nandasena, N., Dyer, B., Sandstrom, M., Stocchi, P., D'Andrea, W., Raymo, M., 2017. Giant boulders and Last Interglacial storm intensity in the North Atlantic. Proc. Natl. Acad. Sci. 114, 12144–12149. https://doi.org/10.1073/pnas.1712433114

Rowe, M., Bristow, C., 2015a. Sea-level controls on carbonate beaches and coastal dunes (eolianite): Lessons from Pleistocene Bermuda. Geol. Soc. Am. Bull. 127, 1645–1665. https://doi.org/10.1130/B31237.1

Rowe, M., Bristow, C.S., 2015b. Landward-advancing Quaternary eolianites of Bermuda. Aeolian Res. 19, 235–249. https://doi.org/10.1016/j.aeolia.2015.06.007

Rutter, N., 1985. Dating methods of Pleistocene deposits and their problems. Geological Association of Canada, Toronto, Ontario.

Rutter, N., Crawford, R., Hamilton, R., 1979. Dating methods of Pleistocene deposits and their problems: IV. Amino acid racemization dating. Geosci. Can. 6.

Schwartz, R., 1982. Bedform and stratification characteristics of some modern small-scale washover sand bodies. Sedimentology 29, 835–849.

Scussolini, P., Bakker, P., Guo, C., Stepanek, C., Zhang, Q., Braconnot, P., Cao, J., Guarino, M.-V., Coumou, D., Prange, M., Ward, P.J., Renssen, H., Kageyama, M., Otto-Bliesner, B., Aerts, J.C.J.H., 2019. Agreement between reconstructed and modeled boreal precipitation of the Last Interglacial. Sci. Adv. 5, eaax7047. https://doi.org/10.1126/sciadv.aax7047

Sealey, N., 2006. Bahamian landscapes: an introduction to the geology and physical geography of the Bahamas, Macmillan Education. ed.

Shinn, E., 1983. Birdseyes, Fenestrae, Shrinkage Pores, and Loferites: A Reevaluation. SEPM J. Sediment. Res. Vol. 53. https://doi.org/10.1306/212F8247-2B24-11D7-8648000102C1865D

Shinn, E., 1968. Practical significance of birdseye structures in carbonate rocks. J. Sediment. Res. 38.

Skrivanek, A., Li, J., Dutton, A., 2018. Relative sea-level change during the Last Interglacial as recorded in Bahamian fossil reefs. Quat. Sci. Rev. 200, 160–177. https://doi.org/10.1016/j.quascirev.2018.09.033

Stieglitz, R., Inden, R., 1969. Development of cavernous sediment in a non-beach environment. J. Sediment. Res. 39, 342–344.

Thompson, W.G., Allen Curran, H., Wilson, M.A., White, B., 2011. Sea-level oscillations during the last interglacial highstand recorded by Bahamas corals. Nat. Geosci. 4, 684–687. https://doi.org/10.1038/ngeo1253

Tormey, B., 1999. A thesis submitted to the faculty of the University of North Carolina at Chapel Hill in partial fulfillment of the requirements for the degree of Master of Science in the Department of Geological Sciences. 154.

Tormey, B.R., Donovan, B.G., Hearty, P.J., 2016. Superstorms of the Last Interglacial: The record from carbonate eolianites of the Bahamas. Presented at the 65th Annual Southeastern GSA Section Meeting. https://doi.org/10.1130/abs/2016SE-273957

Tormey, B.R., Hearty, P.J., Donovan, B.G., 2018. Superstorms deposits in the Bahamas; a record of climate instability from Eleuthera Island during the early peak Last Interglacial (MIS 5e). Presented at the 67th Annual Southeastern GSA Section Meeting - 2018. https://doi.org/10.1130/abs/2018SE-312757

Tormey, D., Donovan, B., 2015. Run over, run up and run out: a storm wave origin for fenestral porosity in last interglacial eolianites of the Bahamas. GSA Abstr. Programs 47.

Tsoar, H., Blumberg, D., 2002. Formation of parabolic dunes from barchan and transverse dunes along Israel's Mediterranean coast. Earth Surf. Process. Landf. 27, 1147–1161. https://doi.org/10.1002/esp.417

Vimpere, L., Kindler, P., Castelltort, S., 2019. Chevrons: Origin and relevance for the reconstruction of past wind regimes. Earth-Sci. Rev. 193, 317–332. https://doi.org/10.1016/j.earscirev.2019.04.005

Viret, G., 2008. Mégablocs au nord d'Eleuthera (Bahamas): preuve de vagues extrêmes au sous-stade isotopique 5e ou restes érosionnels ? (MSc Thesis). University of Geneva, Switzerland.

Walker, M., 2005. Quaternary dating methods. J. Wiley, Chichester, West Sussex, England.

Wanless, H., Dravis, J., Tedesco, L., Rossinsky Jr, V., 1989. Carbonate Environments and Sequences of Caicos Platform, International Geological Congress Field Trip Guidebook.

Whitacre, K., Kaufman, D., Kosnik, M., Hearty, P., 2017. Converting A/I values (ion exchange) to D/L values (reverse phase) for amino acid geochronology. Quat. Geochronol. 37, 1–6. https://doi.org/10.1016/j.quageo.2016.10.004

White, B., Curran, H., 1989. The Holocene Carbonate Eolianites of North Point and the Modern Environments between North Point and Cut Cay, San Salvador Island, Bahamas. pp. 17–22. https://doi.org/10.1029/FT175p0017

Williams, H.F.L., 2011. Shell bed tempestites in the Chenier Plain of Louisiana: late Holocene example and modern analogue. J. Quat. Sci. 26, 199–206. https://doi.org/10.1002/jqs.1444

Wilson, A., 1964. Origin of ice ages: an ice shelf theory for Pleistocene glaciation 3.

Wolcott, D., Donner, D., Brown, D., Ribic, C., 2018. Kirtland's warbler winter habitat changes across the Bahamian Archipelago in response to future climate-condition scenarios. Caribb. Nat. 1–20.

Yan, N., Baas, A., 2015. Parabolic dunes and their transformations under environmental and climatic changes: Towards a conceptual framework for understanding and prediction. Glob. Planet. Change 124, 123–148. https://doi.org/10.1016/j.gloplacha.2014.11.010

Zhuravleva, A., Bauch, H.A., 2018. Last interglacial ocean changes in the Bahamas: climate teleconnections between low and high latitudes. Clim. Past 14, 1361–1375. https://doi.org/10.5194/cp-14-1361-2018

FIGURE AND TABLE CAPTIONS

Table 1: Amino-acid racemization (AAR) ratios measured on 'chevron' samples from Great Exuma and Long Island and obtained by reverse phase (RP) chromatography. Alloisoleucine/Isoleucine (A/I) values were calculated following a log2 transformation of the DL-Glu ratios, following to the method developed by Whitacre *et al.* (2017). The AAR database developed for the Bahamas (Hearty & Kaufman, 2009) was used to corelate the A/I ratios to the corresponding phases of the MIS 5e.

Figure 1: Google Earth© satellite image of the Bahamas showing the location of the four studied islands.

Figure 2: Stratigraphy of the Bahamas islands and its relationship to sea level during the Last Interglacial (LIG). Description of the eustatic phases and ages correspond to the sea-level curve proposed by Godefroid (2012). Note that the boundaries between members cannot be attributed precisely to a specific sea-level stand.

Figure 3: Illustrative sketch of an ideal parabolic dune showing the different morphological parameters measured.

Figure 4: **(A)** Digital elevation model (DEM) of the area near North Eleuthera Airport showing the location of the two sections describing alleged 'chevron' arms (ELI and EAJ; e.g. Hearty *et al.*, 1998). No characteristic U-shaped or V-shaped morphologies are discernible. See text for more explanations. **(B)** DEM of the area near Rock Sound Airport, South Eleuthera, where 'chevrons' have been identified (e.g. Hearty *et al.*, 1998). No characteristic U-shaped or V-shaped morphologies are visible. See text for more explanations.

Figure 5: Digital elevation models (DEMs) showing 'chevron' morphologies: **(A)** on the northern part of Great Exuma (EFH = Farmer's Hill section; ERP = Rokers Point Settlement section); **(B)** at the Michelson section (EMI) on the southern portion of Great Exuma; **(C)** near Miller's Settlement on Long Island (LMI; e.g. Hearty *et al.*, 1998); **(D)** near Old Gray's Settlement in the central part of Long Island (LOG; e.g. Hearty *et al.*, 1998); and **(F)** on Acklins Island where no field data were collected. Refer to text for more details.

Figure 6: Four examples of the studied 95 parabolic dunes around the world. Note the exceptional dimensions of the coastal dunes in Brazil and along the east coast of Australia (C) and

(D), compared to the ones developing on the eastern coast of the USA (A) and (B). The former are more elongated with a narrower deflation basin at their centres whereas the latter are flat-lying, splayed landforms.

Figure 7: Sketches showing two examples of the internal architecture of 'chevron' arms; both exposures are located on Long Island: **(A)** Miller's Settlement (LMI, Fig. 4C); **(B)** Old Gray's Settlement (LOG, Fig. 5D). Note the marked difference in slope angle between the outer and the inner flanks. Sections are retrieved from the DEM and represent the actual morphology of 'chevrons' arms.

Figure 8: 'Chevron' arm sections (A) and (B) usually display low-angle to sub-horizontal aggrading beds (red dashed lines) and bounding surfaces (black dashed lines). **(A)** Arm section LMI (Fig. 5C) where a long-term exposure surface cross-cuts the general bedding and shows early signs of pedogenesis (white dashed line). Outcrop is *ca* 5 m high. **(B)** Arm section ERP (Fig. 5A) showing short-term reactivation surfaces delimitating sets of cross-strata. Outcrop is approximatively 4 m high. **(C)** Arm section LOG (Fig. 5D) showing steep (22°) foresets dipping south. Their orientation indicates a development of the arm perpendicular to the main axis of the ridge. All AAR ratios obtained in these sections correlate with MIS 5e (red: this study; blue: Hearty *et al.*, 1998). Outcrop is *ca* 4 m high. **(D)** View of an arm section (EMI, Fig. 5B) close to the apex of the ridge, showing steep foresets (27°); the dip direction indicates a migration towards the south-west. Outcrop is *ca* 3 m high. **(E)** View of a nose section from Great Exuma (EFH, Fig. 5A); steep (29°) foresets, dipping towards the south-west and aligned with the ridge axis, are visible all along the exposure. Outcrop is *ca* 3 m high.

Figure 9: **(A)** A thin bed showing the association of fenestrae (white triangles) cross-cutting climbing translatent stratification (CTS), bounded by highly cemented laminae. Below and above, grainfall lamination of sub-horizontal aggrading beds are visible. **(B)** Grainfall–sandflow laminae alternation composing the low-angle bedding of the arm section, with some reactivation surfaces. (**C)** Alternation of grainfall and sandflow laminae within foresets. **(D)** Topsets truncating underlying foresets (EX15; N 23°27'47.12"; W 75°43'55.98") where high-angle asymmetrical folds correspond to the basal layer of a slumping sandflow lobe (McKee, 1966; Mckee & Bigarella, 1972; Pye & Tsoar, 2008). The pen and the hammer used for scale in photographs are 15 cm and 33 cm long, respectively.

Figure 10: **(A)** Thin-section view of fenestrae (white arrows) and the alternating grainfall–sandflow laminae in 'chevron' arms (EX11; ERP section). **(B)** Thin-section view of climbing translatent stratification (CTS) in an aeolianite on Long Island (LV18; N 23° 5'57.24"; W 74°59'19.20"). Unlike grainfall–sandflow sets, there is an inverse grain-size gradient within each lamina, the basal section of which (finer part) is usually highly cemented compared to the top one (coarser part). Fenestrae are also frequent in these aeolian deposits (white arrow). **(C), (D) and (E)** Moderately sorted beach-to-intertidal deposits of MIS 5e age from: (C) the Boiling Hole (EL1; N 25°25'41.46"; W 76°35'18.60") and (D) Gregory Town (EL21; N 25°24'33.00"; W 76°33'17.22") on Eleuthera; (E) intertidal deposits on Long Island (LI146; N 23°32'5.54 ; W 75°15'13.33"). (C) Shows a well-preserved fenestral porosity with a complete cementation by sparite, illustrating a freshwater phreatic environment. (D) Presents a higher skeletal content and a coarser grain size than aeolian and 'chevron' deposits. The first generation of bladed isopachous cement (BI) and the following pore-filling equigranular sparite (EC) are indicators of first a marine phreatic, and then a freshwater environment. (E) Displays grains that are first bound by a typical marine phreatic cement (i.e. fibrous isopachous; FI), here followed by a sparitic one (EC). Fenestrae are typical of this kind of environment (white arrows). **(F)** Close-up showing the typical petrography of a 'chevron' arm outer flank (LI107; LOG section). Note the predominance of ooids and peloids versus bioclasts; the latter are mostly represented by *Halimeda* sp. (blank triangles) and *Archaias* sp. (black triangle). Grains are connected by meniscus cement (MC), indicating a vadose environment.

Figure 11: Comparative plots of 'chevron' (green squares; this study) versus parabolic-dune (white circles; data from Appendix 2) morphological parameters. **(A)** L/W plot: parabolic aeolian dunes and 'chevrons' are either lobate or elongated according to Pye's (1993) classification of simple parabolic dunes. The elongation (L/W) of all measured ridges follows a linear law with a good level of confidence. **(B)** L/H plot: it represents the flatness of the studied landforms and shows a scattered population with rather flat 'chevrons'. **(C)** φ/α plot: the stoss-slope angle (φ) increases exponentially with the lee-face angle (α) for all V-shaped ridges. **(D)** W/H plot: it shows a scattered population where 'chevrons' are among the widest landforms compared to their heights.

Figure 12: Examples of storm deposits of Recent, Holocene, and Late Pleistocene age. **(A)** Satellite view of partly quarried, recent, sandy to conglomeratic washover deposits capping a sea cliff *ca* 1 km to the south-east of Boiling Hole (Eleuthera). Coordinates: N 25°25'36.48"; W 76°35'21.89". Note lobe shape of deposits. Image Google Earth©. **(B)** Conglomeratic storm berm along the southern coast of Great Inagua. Coordinates: N 20°55'28.99"; W 73°30'3.89". Clasts mostly consist of decimetre-sized coral debris derived from an adjacent reef. Top of the berm is about 2.5 m above sea level. Bush on the left is *ca.* 1 m high. **(C)** Coastal exposure along the coastline of Flamingo Bay (Mayaguana). Coordinates: N 22°24'31.85"; W 72°59'15.00". Outcrop shows a shallowing-upward succession of beach and dune deposits of Holocene age (Hanna Bay Formation). A boulder layer representing a fossil storm berm is interstratified between the beach and the dune deposits. White rectangle shows the position of (D). Hammer is 35 cm long. Top of the exposure is *ca* 2 m above sea level. **(D)** Close-up view of the boulder layer mentioned in (C). Hammer is 35 cm long. **(E)** Roadcut leading to Rainbow Beach (Eleuthera). Coordinates: N 25°20'2.33"; W 76°25'53.01". Exposure consists of coarse to very coarse, sandy oolitic deposits of MIS 5e age. Coarse grain size, predominant subhorizontal stratifications and small antidunes identify these beds as fossil washover deposits. Interestingly, sediments came from the open sea located to the left and were transported bankward (i.e. to the right) into a lagoon. These deposits overlie bioturbated lagoonal sediments (not visible on the photograph). Bag for scale is 50 cm high. Black rectangle shows the position of (F). (**F)** Close-up view of small antidune in MIS 5e washover deposits. Flow moved from left to right. Structure behind the coin (diameter of 1.9 cm for scale) is a rhizolith.

Figure 13: Arm sections described in aeolian parabolic dunes from Canada and Brazil. Similarities with 'chevron' arms (Fig. 7) include an outer flank generally steeper than the flank facing the deflation basin, cross-bed sets dipping towards the outside, and an analogous size.

Figure 14: **(A)** Typical morphology and internal structure of washover fans deposited on a hard substrate. They present a thinning-landward lobe shape, with a sub-horizontal stratification. Several lobes can be superimposed or found interfingering with aeolian sediments. **(B)** Reconstruction of the internal structure of 'chevrons', based on the different sections observed in the field, and shown as a strike view through an arm and the nose. Note the greater complexity of these deposits when compared with typical aeolian features.

Figure 15: **(A)** Cumulative frequency curves of grain-size populations measured for 'chevrons' (green lines), aeolianites (black lines) and beach deposits (orange lines). The latter are composed of coarser sediments, whereas 'chevrons' and aeolian dunes show a similar distribution. **(B)** The distribution type is more easily read on a frequency plot. 'Chevrons' and aeolianites have a bimodal distribution, whereas beaches show a polymodal distribution. Values at dashed lines show the common modes between types of deposits, indicating a reworking of material of one by the other, or a common source.

APPENDICES CAPTIONS

Appendix 1: Morphological parameters measured on Bahamian 'chevrons'.

Appendix 2: Morphological parameters measured on 95 parabolic dunes around the world.

Appendix 3: Grain-size classification implanted in GRADISTAT v.8 and used in this study.

Appendix 4: DEM of Long Island showing the locations of all the 'chevrons' for which morphological parameters have been measured (see Appendix 1).

Appendix 5: Statistics obtained with the Excel macro GRADISTAT v.8 (Blott & Pye, 2001) on the grain-size distributions of 'chevrons', aeolianites and beaches by applying the Folk & Ward (1957) method.

Sample #	DL Asp	DL Glu	DL Ser	DL Ala	DL Val	DL Phe
EX10	0.478 ±0.010	0.445 ±0.003	0.388 ±0.008	0.728 ±0.008	0.388 ±0.006	0.509 ±0.004
EX11	0.455 ±0.016	0.424 ±0.005	0.349 ±0.025	0.691 ±0.006	0.370 ±0.012	0.520 ±0.032
LI107	0.492 ±0.004	0.413 ±0.009	0.254 ±0.097	0.665 ±0.012	0.340 ±0.006	0.439 ±0.005
LI133	0.520 ±0.006	0.461 ±0.001	0.364 ±0.025	0.775 ±0.015	0.419 ±0.002	0.521 ±0.019

DL Ile	DL Leu	A/I calculated from DL-Glu	Associated MIS
0.345 ±0.004	0.661 ±0.003	0.453 ±0.003	Early 5e
0.353 ±0.037	0.667 ±0.032	0.414 ±0.005	Latest 5e
0.295 ±0.011	0.587 ±0.045	0.394 ±0.009	Latest 5e
0.390 ±0.035	0.704 ±0.017	0.483 ±0.001	Early 5e

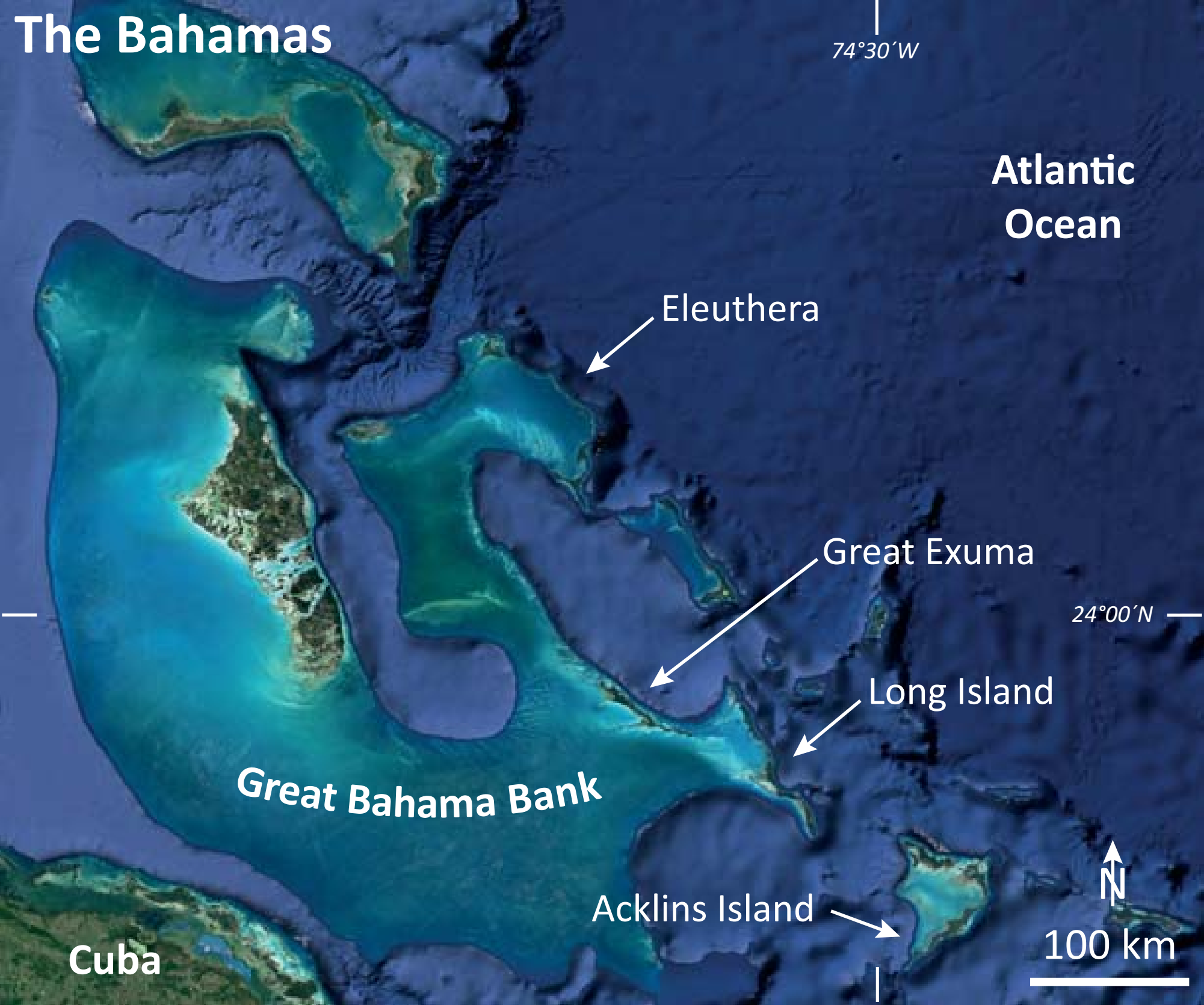
The Bahamas
74°30´W
Atlantic Ocean
Eleuthera
Great Exuma
24°00´N
Long Island
Great Bahama Bank
Acklins Island
Cuba
N
100 km

Age	MIS	Formation	Member
Holocene	1	Rice Bay	*Hanna Bay*
	Mid. 1		*North Point*
Late Pleistocene	3	N/A	
	5a	Whale Point	
	5e	Grotto Beach	*Big Cove*
			Cockburn Town
			French Bay
Middle Pleistocene	7	Owl's Hole	
	9/11		
	13		
	15 to 19		

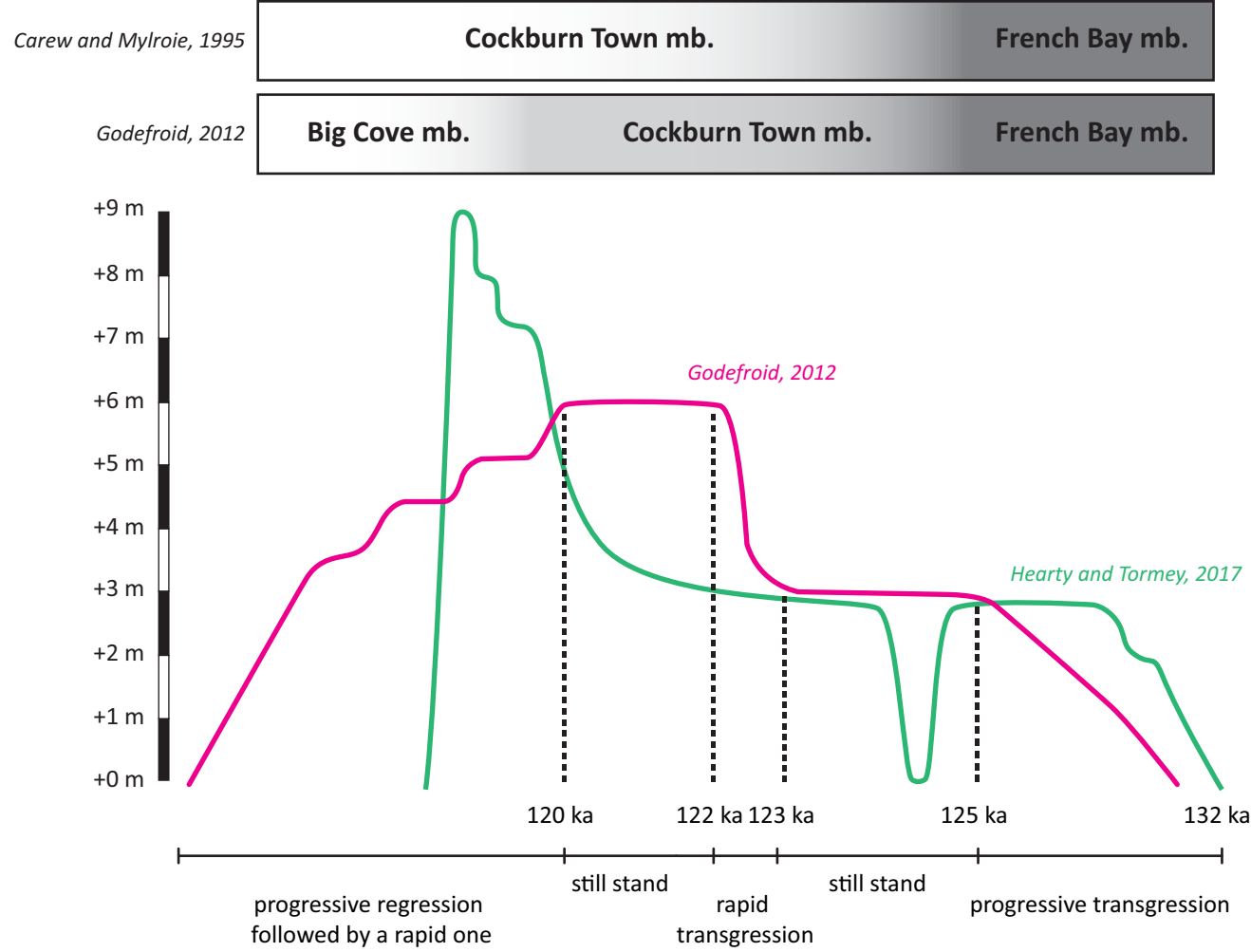

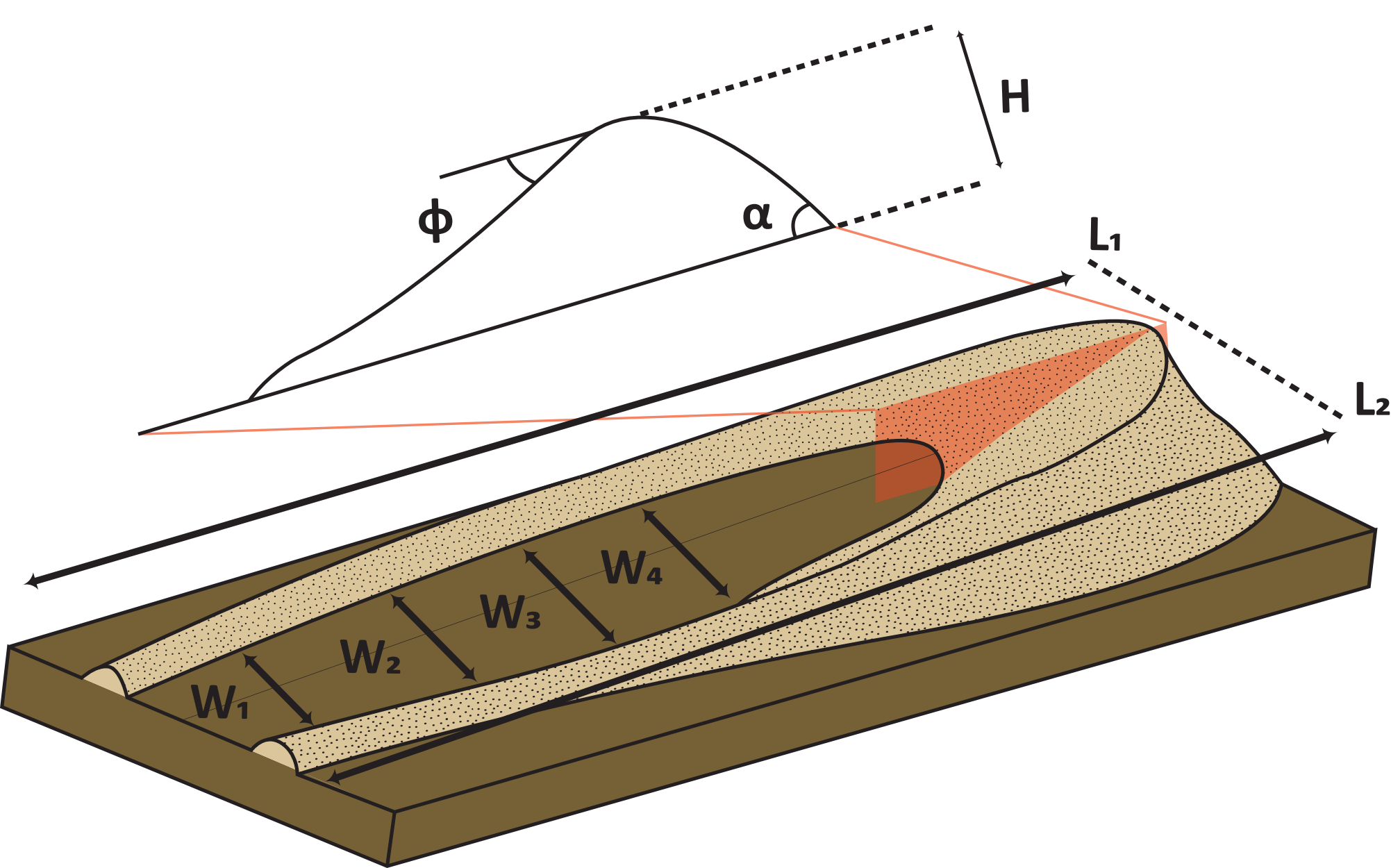
H
ϕ
α
L1
L2
W1
W2
W3
W4

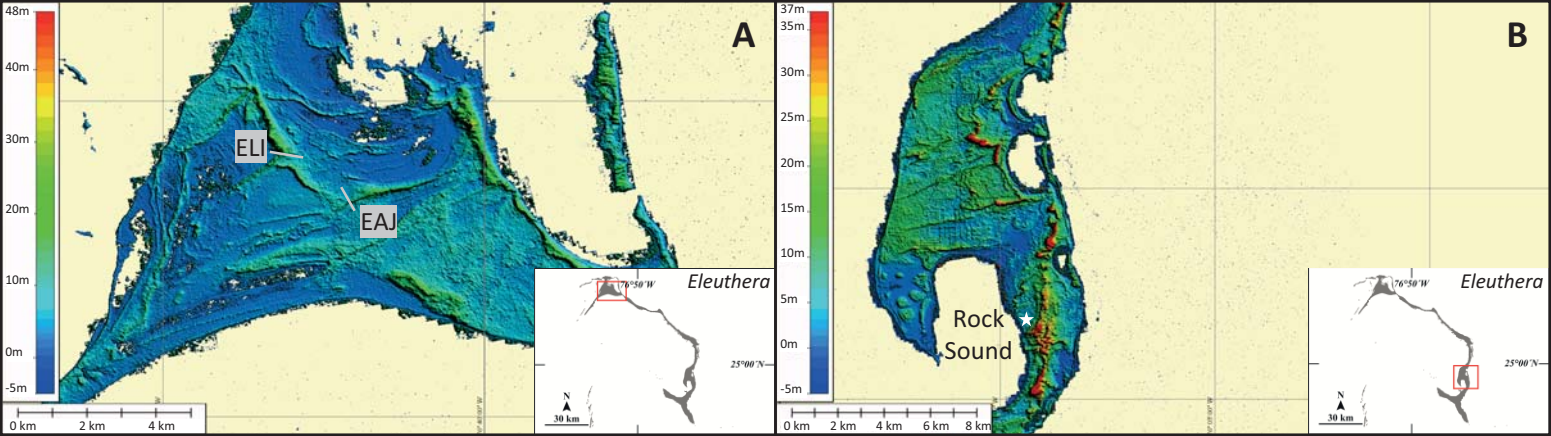
A
48m
40m
30m
20m
10m
0m
-5m
ELI
EAJ
0 km
2 km
4 km
76°50'W
25°00'N
Eleuthera
N
30 km
B
37m
35m
30m
25m
20m
15m
10m
5m
0m
-5m
Rock
Sound
0 km
2 km
4 km
6 km
8 km
76°50'W
25°00'N
Eleuthera
N
30 km

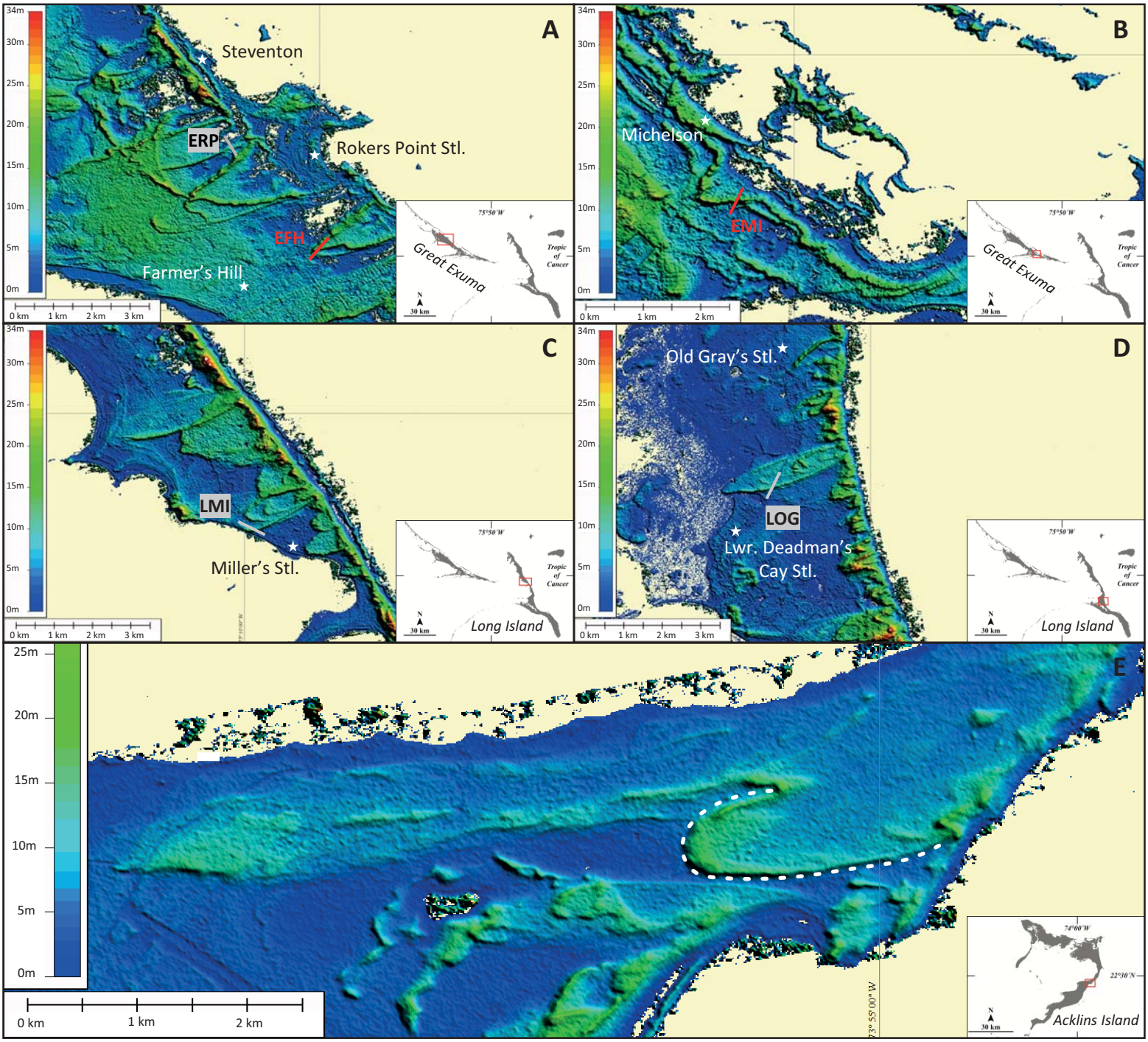
A
Steventon
ERP
Rokers Point Stl.
EFH
Farmer's Hill
B
Michelson
EMI
C
LMI
Miller's Stl.
D
Old Gray's Stl.
LOG
Lwr. Deadman's Cay Stl.
E
Great Exuma
Long Island
Acklins Island
Tropic of Cancer
34m
30m
25m
20m
15m
10m
5m
0m
0 km
1 km
2 km
3 km
30 km
75°50'W
74°00'W
22°30'N
73° 55' 00" W

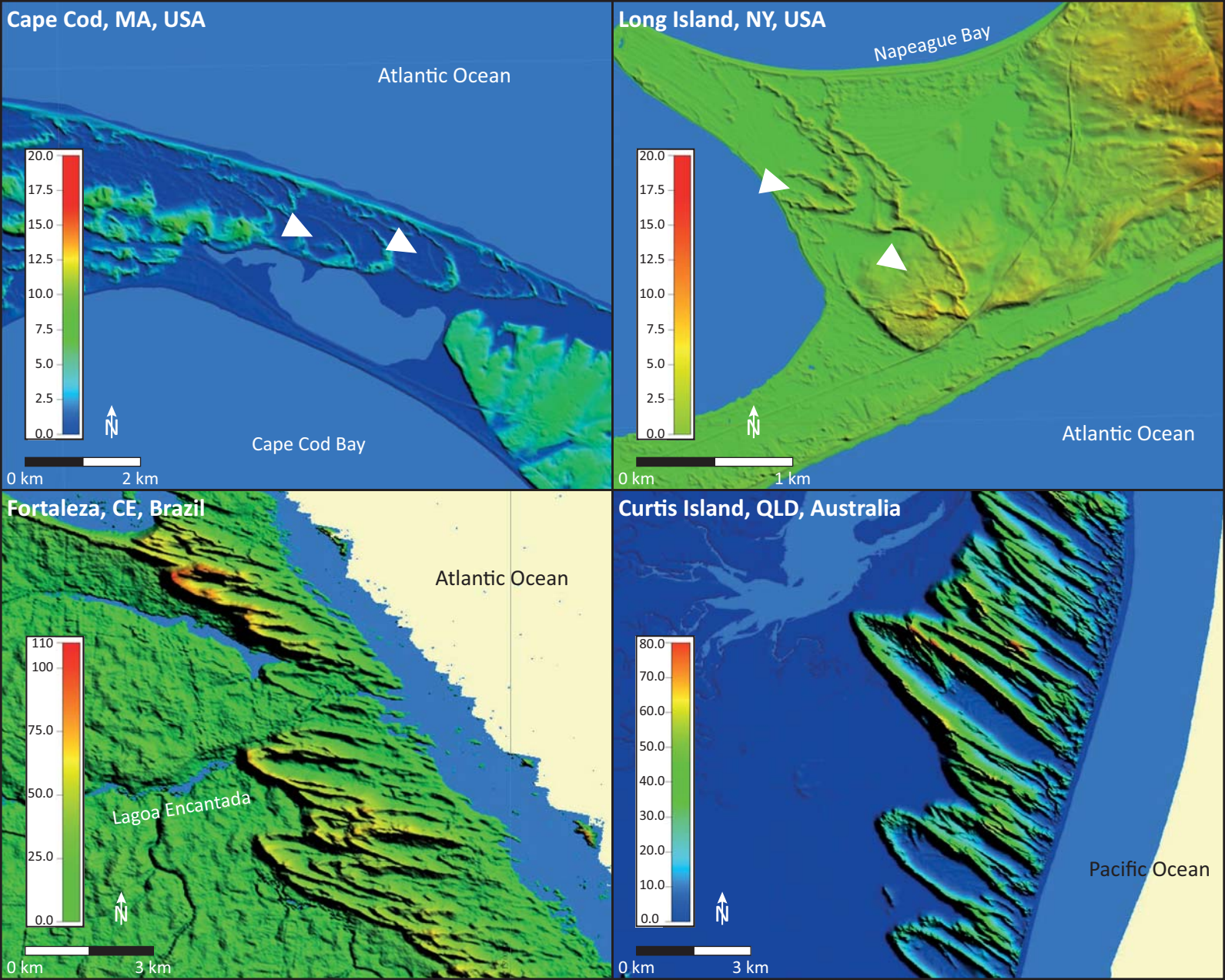
Cape Cod, MA, USA
Atlantic Ocean
Cape Cod Bay
20.0
17.5
15.0
12.5
10.0
7.5
5.0
2.5
0.0
N
0 km
2 km
Long Island, NY, USA
Napeague Bay
Atlantic Ocean
20.0
17.5
15.0
12.5
10.0
7.5
5.0
2.5
0.0
N
0 km
1 km
Fortaleza, CE, Brazil
Atlantic Ocean
Lagoa Encantada
110
100
75.0
50.0
25.0
0.0
N
0 km
3 km
Curtis Island, QLD, Australia
Pacific Ocean
80.0
70.0
60.0
50.0
40.0
30.0
20.0
10.0
0.0
N
0 km
3 km

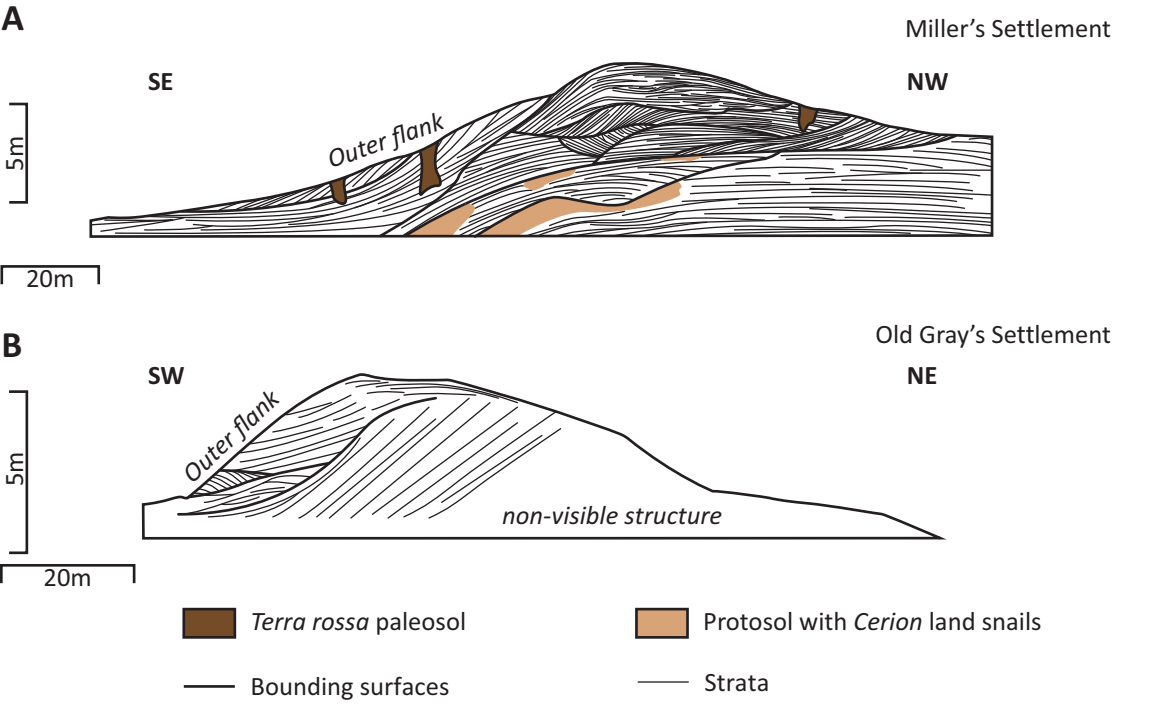
A
Miller's Settlement
SE
NW
5m
Outer flank
20m
B
Old Gray's Settlement
SW
NE
5m
Outer flank
non-visible structure
20m
Terra rossa paleosol
Protosol with Cerion land snails
Bounding surfaces
Strata

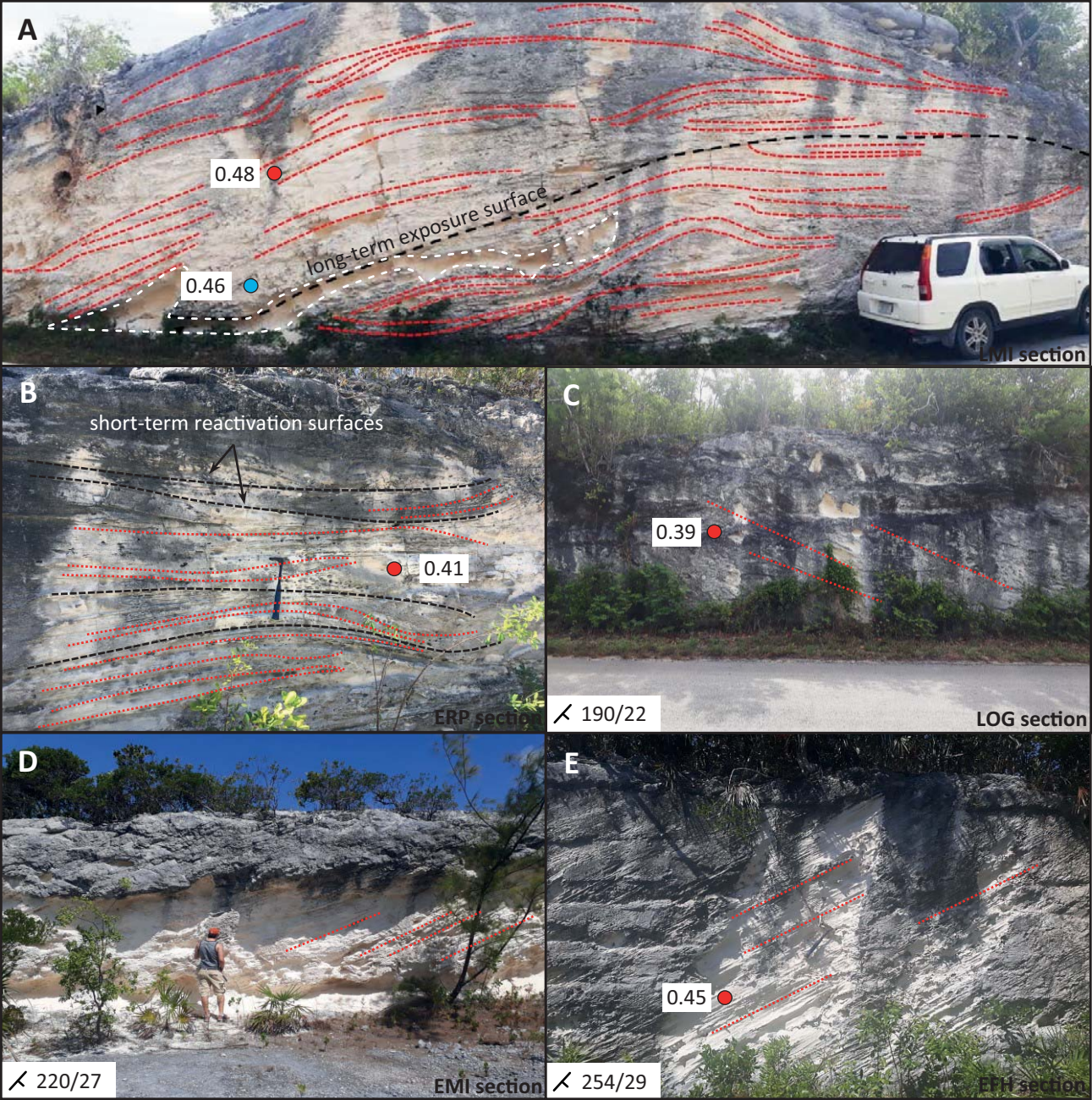
A
0.48
long-term exposure surface
0.46
EMI section
B
short-term reactivation surfaces
0.41
ERP section
C
0.39
190/22
LOG section
D
220/27
EMI section
E
0.45
254/29
ETH section

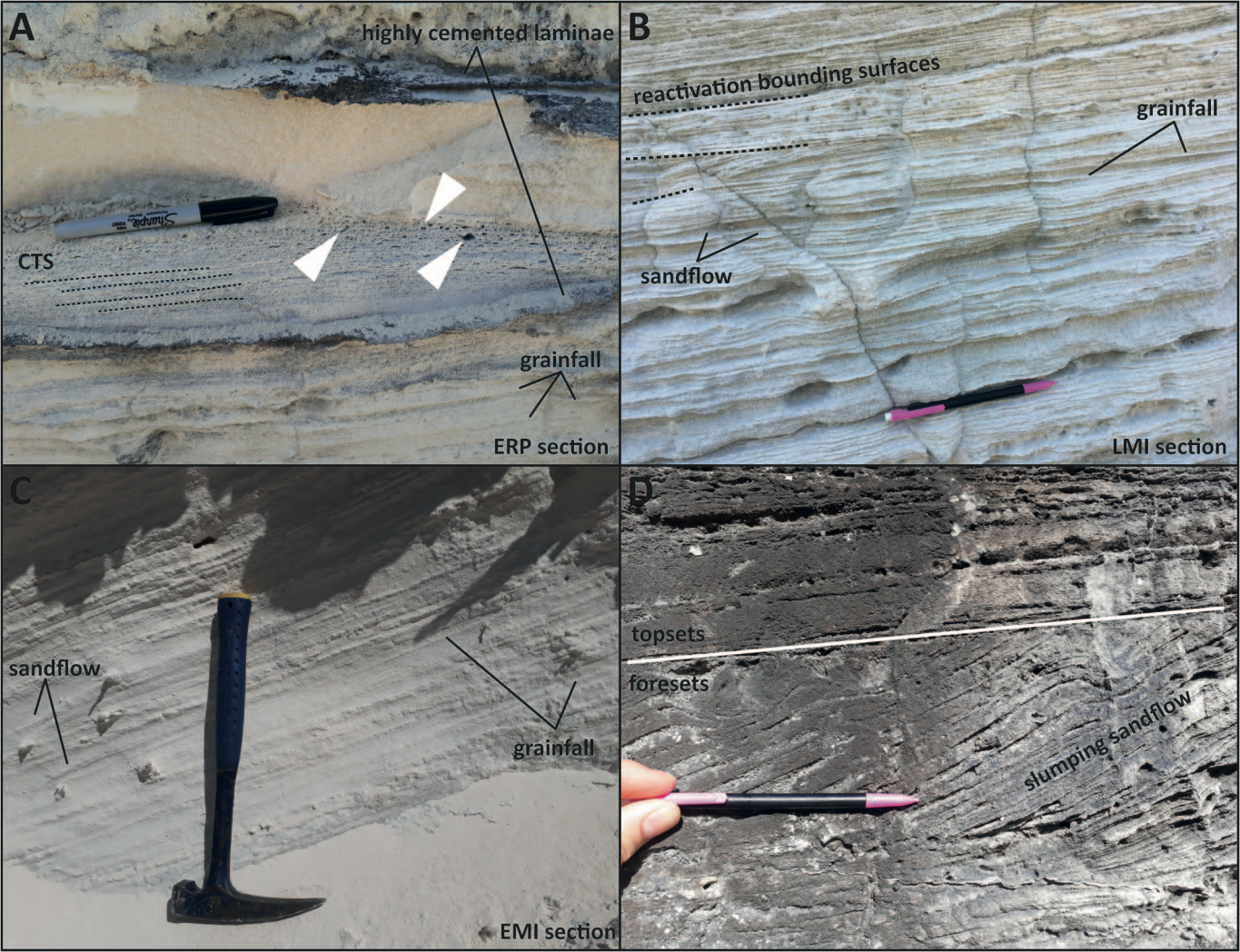
A
highly cemented laminae
CTS
grainfall
ERP section
B
reactivation bounding surfaces
grainfall
sandflow
LMI section
C
sandflow
grainfall
EMI section
D
topsets
foresets
slumping sandflow

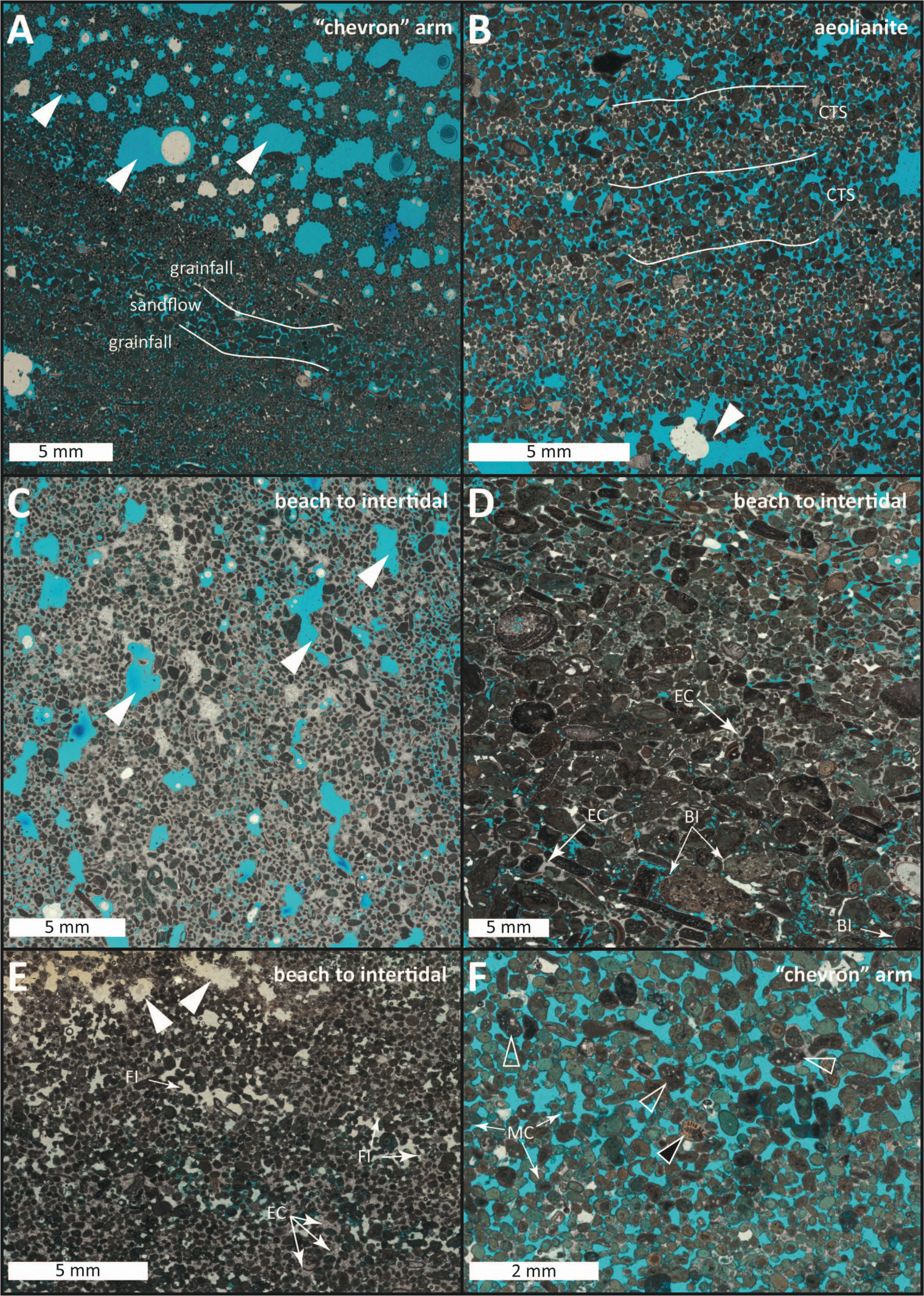
A
"chevron" arm
grainfall
sandflow
grainfall
5 mm
B
aeolianite
CTS
CTS
5 mm
C
beach to intertidal
5 mm
D
beach to intertidal
EC
EC
BI
5 mm
BI
E
beach to intertidal
FI
FI
EC
5 mm
F
"chevron" arm
MC
2 mm

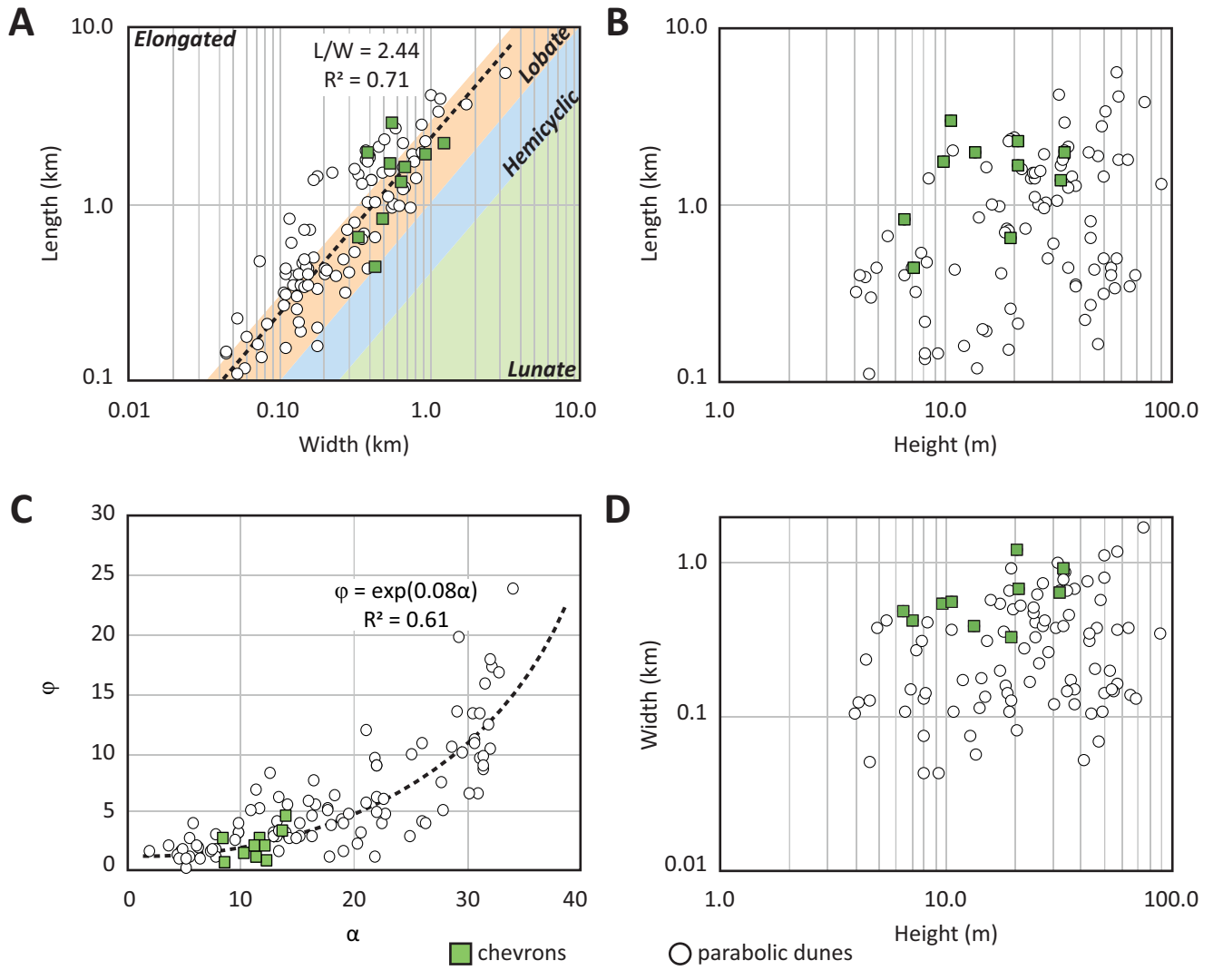
A
Elongated
L/W = 2.44
R² = 0.71
Lobate
Hemicyclic
Lunate
Length (km)
Width (km)
10.0
1.0
0.1
0.01
0.10
1.0
10.0
B
Length (km)
Height (m)
1.0
10.0
100.0
C
φ = exp(0.08α)
R² = 0.61
φ
α
30
25
20
15
10
5
0
40
chevrons
D
Width (km)
0.01
parabolic dunes


Pleistocene
aeolianite
washover
deposits
Pleistocene
aeolianite
N
100 m
A


B

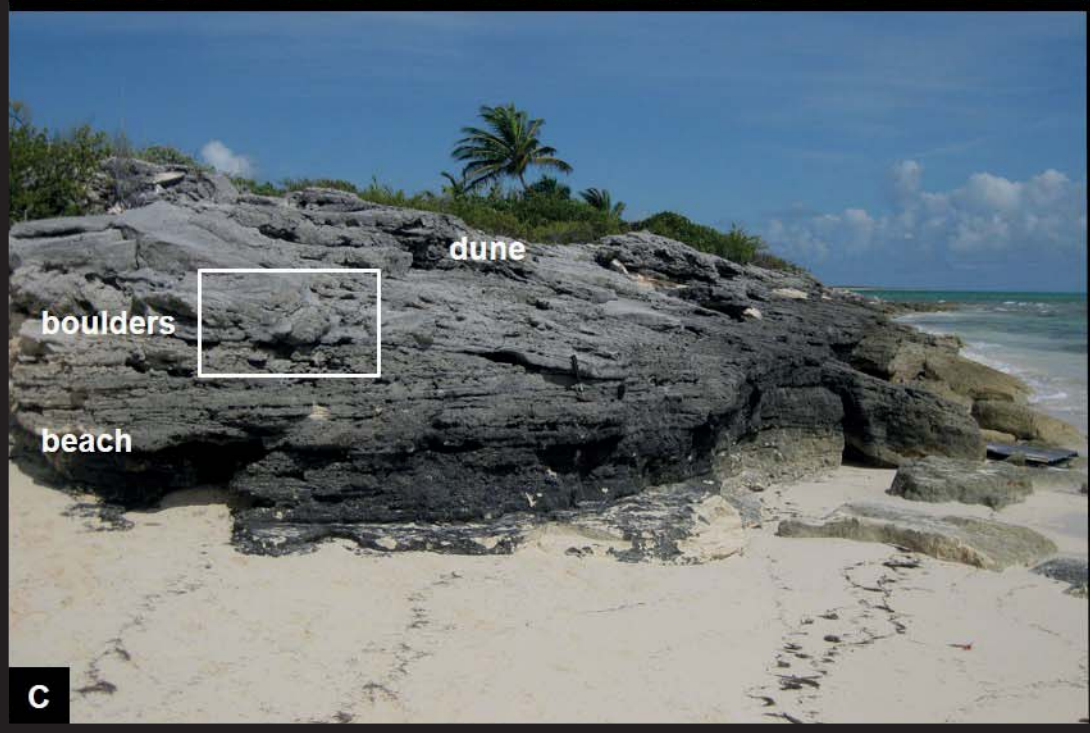
dune
boulders
beach
C

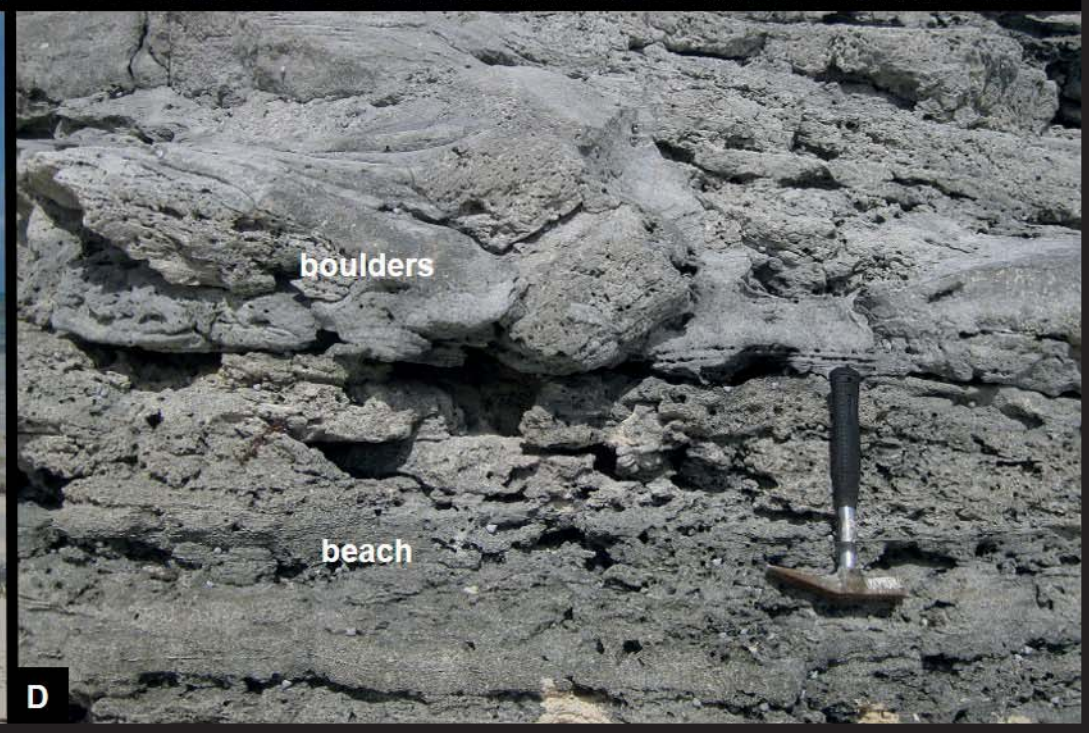
boulders
beach
D


E


F

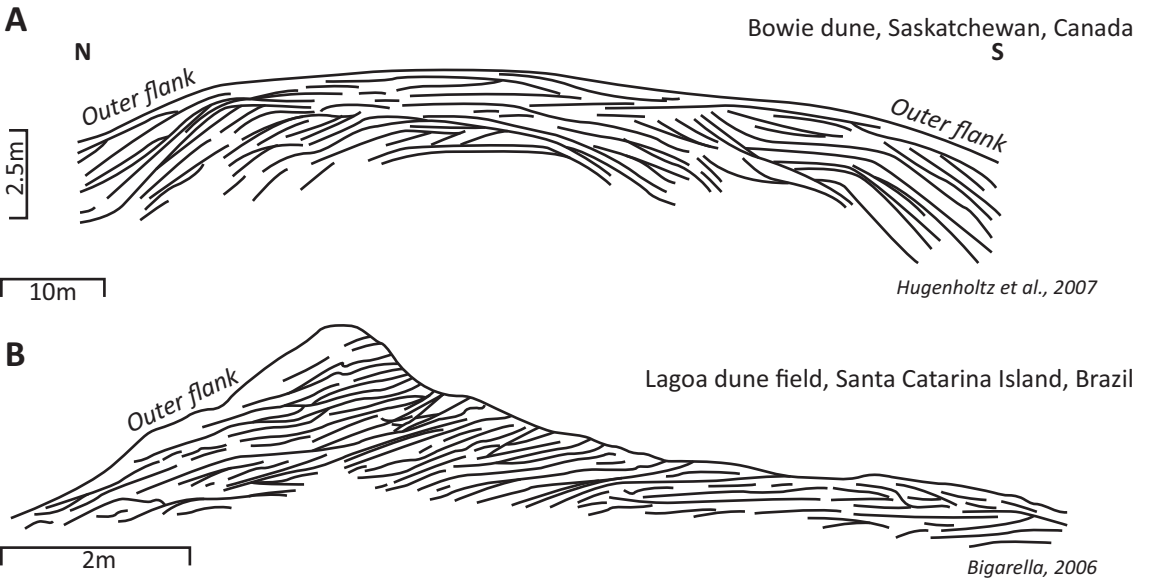
A
Bowie dune, Saskatchewan, Canada
N
S
Outer flank
Outer flank
2.5m
10m
Hugenholtz et al., 2007
B
Lagoa dune field, Santa Catarina Island, Brazil
Outer flank
2m
Bigarella, 2006

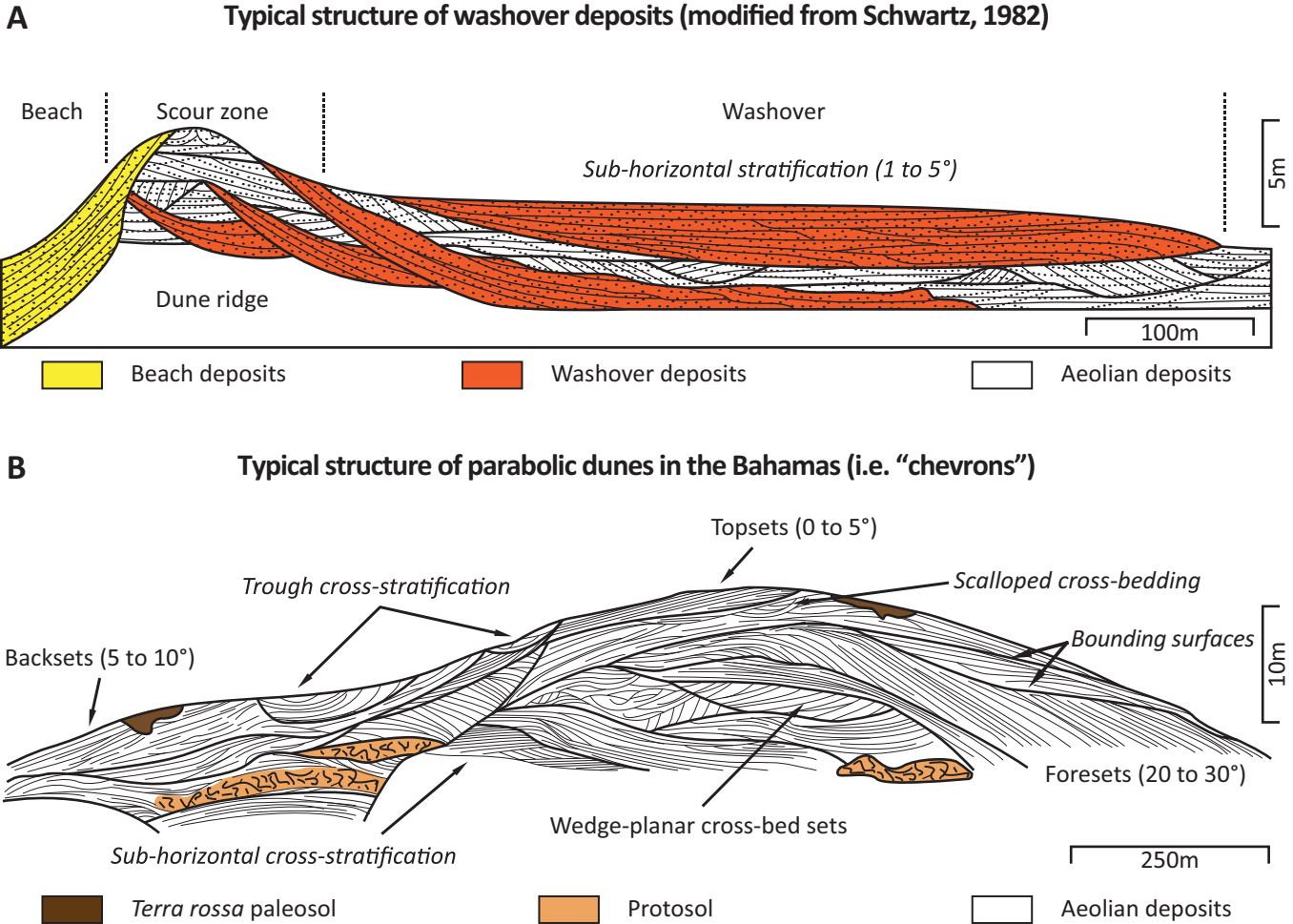
A
Typical structure of washover deposits (modified from Schwartz, 1982)
Beach
Scour zone
Washover
Sub-horizontal stratification (1 to 5°)
5m
Dune ridge
100m
Beach deposits
Washover deposits
Aeolian deposits
B
Typical structure of parabolic dunes in the Bahamas (i.e. "chevrons")
Topsets (0 to 5°)
Trough cross-stratification
Scalloped cross-bedding
Backsets (5 to 10°)
Bounding surfaces
10m
Foresets (20 to 30°)
Wedge-planar cross-bed sets
Sub-horizontal cross-stratification
250m
Terra rossa paleosol
Protosol
Aeolian deposits

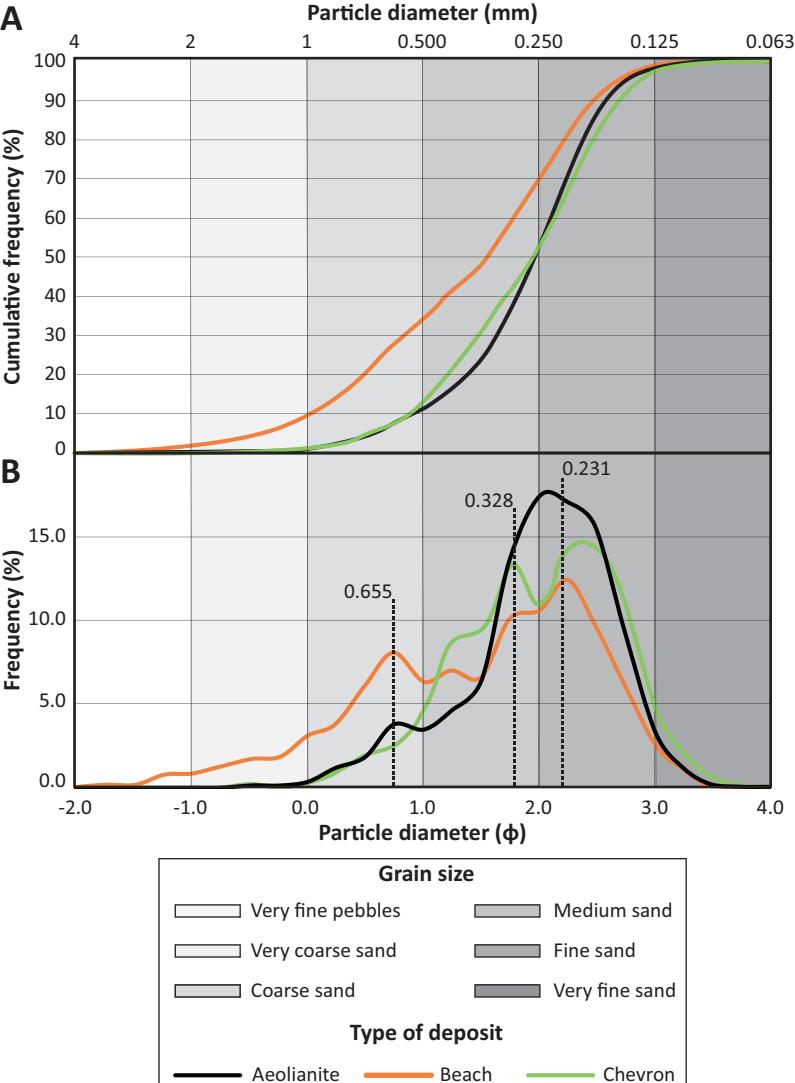
A
Particle diameter (mm)
4
2
1
0.500
0.250
0.125
0.063
Cumulative frequency (%)
100
90
80
70
60
50
40
30
20
10
0
B
0.231
0.328
0.655
Frequency (%)
15.0
10.0
5.0
0.0
-2.0
-1.0
0.0
1.0
2.0
3.0
4.0
Particle diameter (ϕ)
Grain size
Very fine pebbles
Very coarse sand
Coarse sand
Medium sand
Fine sand
Very fine sand
Type of deposit
Aeolianite
Beach
Chevron

Country	Location	#	Latitude	Longitude	Length (km)	Width (km)
Bahamas	Acklins Island	BA-AK-1	-73.92076549	22.4541297	1.7	0.7
	Great Exuma	BA-EX-1	23.60059532	-75.90942285	2.0	0.9
		BA-EX-2	23.61302144	-75.93386116	2.3	1.2
	Long Island	BA-LI-1	23.39387798	-75.15983993	1.7	0.5
		BA-LI-2	23.39033623	-75.14889872	0.4	0.4
		BA-LI-3	23.38525569	-75.1477418	0.8	0.5
		BA-LI-4	23.20854549	-75.10488345	3.0	0.6
		BA-LI-5	23.49180939	-75.21479271	2.0	0.4
		BA-LI-6	23.49974602	-75.21195173	0.7	0.3
		BA-LI-7	23.55561114	-75.23908522	1.4	0.6

Height (m)	L/W	L/H	W/H	Perimeter (km)	Pile Volume (m3)	Enclosed Area (km2)	α (°)	φ (°)
21	2.5	79.8	32.5	5.192	5.67E+06	1.351	12	1
33	2.1	59.1	27.9	5.589	8.56E+06	1.530	14	3
21	1.8	109.9	60.0	6.993	9.08E+06	2.360	14	5
10	3.2	178.7	56.4	4.267	1.66E+06	1.015	11	2
7	1.0	62.3	60.0	1.647	8.08E+05	0.180	12	3
7	1.7	127.5	74.8	2.689	1.90E+06	0.413	11	1
11	5.3	281.8	53.3	6.732	7.38E+06	1.754	9	1
13	5.1	147.4	28.9	4.959	4.50E+06	0.967	8	3
19	1.9	33.7	17.4	2.202	2.55E+06	0.315	12	2
32	2.1	42.8	20.1	4.281	7.59E+06	0.903	10	2

Country	Location	#	Orientation (°)	Latitude	Longitude
Australia	Brooms Head	A-NSW-BH1	354	-29.69870707	153.304245
	Corio Bay	A-QL-CB1	315	-22.90306142	150.7613663
		A-QL-CB2	306	-22.90031665	150.7732173
		A-QL-CB3	309	-22.89176719	150.7662411
		A-QL-CB4	314	-22.86862496	150.7443581
		A-QL-CB4 Bis	312	-22.87212275	150.747876
		A-QL-CB4 Ter	311	-22.87872555	150.7564263
		A-QL-CB5	308	-22.864335	150.7601711
		A-QL-CB6	309	-22.81853904	150.7472807
		A-QL-CB6 Bis	308	-22.83731873	150.7716576
		A-QL-CB7	312	-22.81731888	150.7822937
	Curtis Island	A-QL-CI1	312	-23.58494078	151.2193205
		A-QL-CI2	309	-23.57235967	151.2181905
		A-QL-CI3	307	-23.56553214	151.2135614
		A-QL-CI4	310	-23.55385426	151.2130352
		A-QL-CI5	310	-23.53239673	151.2104574
	Fraser Island	A-QL-FI4	316	-25.62615708	153.0015535
		A-QL-FI4 Bis	313	-25.66275231	153.0346471
		A-QL-FI5	314	-25.31935612	153.1962913
		A-QL-FI6	321	-25.21866308	153.187241
		A-QL-FI7	320	-24.81071775	153.201982
		A-QL-FI8	314	-24.82422159	153.2484204
	Nigaloo	A-WA-NI1	7	-22.70397667	113.6755808
		A-WA-NI2	5	-22.6969385	113.6842872
		A-WA-NI3	6	-22.70341284	113.6833336
		A-WA-NI4	6	-22.72477998	113.7322529
		A-WA-NI5	15	-22.76130553	113.7659777
		A-WA-NI6	13	-22.77767455	113.7753578
	S Wide Bay	A-QL-FI1	315	-26.11963797	153.0934262
		A-QL-FI2	321	-26.08798022	153.1015954
		A-QL-FI3	326	-25.99924296	153.1330935
Brazil	Fortaleza	BR-NE-FO1	282	-3.974844085	-38.27592687
		BR-NE-FO2	284	-3.954689388	-38.2824318
		BR-NE-FO3	284	-3.925449313	-38.34426684
		BR-NE-FO4	290	-3.841701749	-38.40953705
Denmark	Blåvand	DK-VA-BL1	91	55.562903	8.180225
		DK-VA-BL2	94	55.562903	8.180225
		DK-VA-BL3	112	55.562903	8.180225
		DK-VA-BL4	103	55.562903	8.180225
Lybia	Marsa el Brega	LY-CY-MB1	137	30.54879666	19.82692651
		LY-CY-MB2	118	30.56104774	19.84881889
		LY-CY-MB3	115	30.5876103	19.87671939
		LY-CY-MB4	120	30.57705417	19.93646851
		LY-CY-MB5	113	30.61318917	19.93152778
		LY-CY-MB6	127	30.65424972	19.96097331
		LY-CY-MB7	137	30.76761139	20.03540217
		LY-CY-MB8	123	30.7820648	20.03037896
		LY-CY-MB9	109	30.85132961	20.11861998
Netherlands	Ijmuiden	N-NH-IJ1	60	52.430793	4.582964

Scotland	Newburgh	S-AS-NB1	66	57.329339	-1.980733
		S-AS-NB2	330	57.329339	-1.980733
Spain	Suances	SP-CT-SU1	96	43.44699865	-3.966752388
		SP-CT-SU2	88	43.44466424	-3.971551175
		SP-CT-SU3	107	43.4452077	-3.968852109
USA	Cape Cod	US-MA-CC1	112	42.072854	-70.184356
		US-MA-CC2	109	42.072854	-70.184356
		US-MA-CC3	123	42.072854	-70.184356
		US-MA-CC4	116	42.072854	-70.184356
	Eureka	US-CA-EU1	156	40.833924	-124.178084
		US-CA-EU2	162	40.833924	-124.178084
		US-CA-EU3	167	40.833924	-124.178084
	Grand Marais	US-MI-GM1	135	46.68600171	-85.89501698
	Holland	US-MI-HO1	73	42.759235	-86.203838
		US-MI-HO2	79	42.759235	-86.203838
		US-MI-HO3	81	42.759235	-86.203838
		US-MI-HO4	80	42.759235	-86.203838
		US-MI-HO5	63	42.759235	-86.203838
		US-MI-HO6	75	42.759235	-86.203838
	Lompoc	US-CA-LO1	121	34.80284	-120.590197
		US-CA-LO2	114	34.80284	-120.590197
		US-CA-LO3	102	34.80284	-120.590197
		US-CA-LO4	107	34.80284	-120.590197
	P.J. Hoffmaster	US-MI-PJ1	82	43.131273	-86.273739
		US-MI-PJ2	76	43.131273	-86.273739
		US-MI-PJ3	69	43.131273	-86.273739
	Petoskey	US-MI-PE1	96	45.407558	-84.908026
		US-MI-PE2	81	45.407558	-84.908026
	Point Reyes Seashore	US-CA-PR1	128	38.093631	-122.966166
		US-CA-PR2	128	38.093631	-122.966166
		US-CA-PR3	129	38.093631	-122.966166
	Van Buren	US-MI-VB1	68	42.335358	-86.303944
		US-MI-VB2	69	42.335358	-86.303944
	Warren Dunes	US-MI-WI1	92	41.913434	-86.588026
		US-MI-WI2	97	41.913434	-86.588026
		US-MI-WI3	74	41.913434	-86.588026
		US-MI-WD1	73	41.913434	-86.588026
		US-MI-WD2	81	41.913434	-86.588026
		US-MI-WD3	88	41.913434	-86.588026
		US-MI-WD4	82	41.913434	-86.588026
Wales	Newborough	WA-IA-NB1	23	53.142467	-4.366393
		WA-IA-NB2	22	53.142467	-4.366393
		WA-IA-NB3	24	53.142467	-4.366393
		WA-IA-NB4	22	53.142467	-4.366393
		WA-IA-NB5	25	53.142467	-4.366393
		WA-IA-NB6	53	53.142467	-4.366393

Length (km)	Width (km)	Height (m)	L/W	L/H	W/H	Perimeter (km)
1.5	0.2	36	8.2	40.6	5.0	3.799
1.9	0.4	47	4.8	40.0	8.3	4.722
0.8	0.3	44	2.6	18.4	7.2	2.265
1.8	0.4	58	4.8	31.1	6.5	4.83
2.1	0.5	35	4.6	61.1	13.3	6.334
2.4	0.5	20	4.7	119.8	25.2	6.171
1.1	0.4	31	2.8	34.1	12.3	3.522
2.9	0.9	34	3.3	86.6	26.4	7.55
4.2	1.0	31	4.1	134.7	32.6	11.118
2.0	0.8	43	2.6	46.0	17.8	6.935
1.4	0.2	24	8.3	59.0	7.1	4.159
0.7	0.2	19	4.6	39.3	8.6	2.03
0.7	0.1	19	5.0	38.5	7.7	2.23
1.4	0.4	25	3.4	56.4	16.6	4.038
1.9	0.4	27	4.8	70.3	14.7	5.414
2.7	0.6	49	4.7	56.3	12.0	6.832
5.6	3.2	57	1.8	99.5	56.6	20.439
3.4	1.1	50	3.0	67.1	22.6	12.025
1.4	0.8	50	1.8	28.9	16.2	4.48
4.1	1.2	58	3.4	70.4	20.4	11.649
3.8	1.7	75	2.2	50.3	22.9	18.615
1.7	0.7	32	2.5	51.8	20.8	4.528
1.4	0.4	8	3.4	169.4	49.8	3.907
0.7	0.3	22	2.6	33.0	12.8	2.037
1.0	0.4	27	2.4	38.0	15.7	3.164
0.7	0.4	18	1.9	38.4	20.0	2.127
1.5	0.5	24	3.2	62.6	19.6	4.027
1.5	0.3	25	4.5	60.4	13.6	3.313
1.9	0.4	33	4.8	56.4	11.8	4.786
1.5	0.2	26	6.8	58.9	8.7	4.602
2.0	0.9	33	2.3	59.9	26.6	6.709
1.8	0.4	64	4.7	28.0	6.0	5.055
1.3	0.4	90	3.8	14.7	3.9	3.899
0.5	0.3	28	1.8	17.4	9.4	1.419
0.7	0.4	43	1.8	15.0	8.1	2.624
1.0	0.6	17	1.8	56.6	32.1	2.806
0.3	0.3	7	1.2	43.5	37.0	1.153
1.0	0.6	16	1.7	63.6	36.5	2.979
1.6	0.3	15	5.1	107.5	21.0	4.02
1.8	0.8	33	2.2	53.5	23.9	6.018
1.0	0.6	25	1.6	39.1	24.8	3.1
1.3	0.7	38	1.9	34.2	18.3	0.778
2.3	0.9	19	2.5	120.2	48.7	6.527
2.3	0.7	19	3.4	119.6	35.2	5.747
1.2	0.7	35	1.9	35.9	19.0	3.739
1.1	0.5	24	2.1	45.6	21.4	3.214
1.6	0.5	22	3.0	73.8	24.9	4.732
1.0	0.7	27	1.3	35.6	27.3	3.529
0.4	0.2	18	2.0	23.3	11.5	1.646

0.2	0.2	12	0.9	13.3	14.8	0.765
0.2	0.1	15	1.4	12.9	9.1	0.73
0.2	0.1	8	1.6	27.3	16.6	0.734
0.2	0.1	19	1.4	8.1	5.8	0.611
0.2	0.2	14	1.1	13.9	12.5	0.846
0.4	0.2	4	1.6	90.0	54.6	1.387
0.3	0.1	5	2.3	65.7	28.3	0.922
0.7	0.4	6	1.5	121.1	78.4	2.15
0.4	0.4	5	1.1	89.7	78.0	1.663
0.5	0.3	8	1.7	69.0	40.6	1.634
0.3	0.1	4	3.0	80.6	26.9	0.993
0.4	0.1	4	3.2	96.7	30.4	1.068
0.3	0.1	N/A	2.0	N/A	N/A	0.893
0.4	0.2	54	2.2	8.2	3.7	1.538
0.2	0.1	47	2.3	3.5	1.5	0.602
0.3	0.1	44	2.6	6.2	2.4	0.815
0.3	0.1	49	2.8	6.3	2.2	0.852
0.4	0.1	37	2.9	9.5	3.3	1.055
0.4	0.2	45	2.1	9.4	4.5	1.408
0.4	0.1	7	3.6	61.2	16.8	1.023
0.4	0.2	7	2.9	62.2	21.7	1.213
0.5	0.1	8	3.3	57.9	17.6	1.271
2.0	0.4	11	5.4	192.4	35.5	4.97
0.5	0.2	57	3.0	8.8	2.9	1.677
0.4	0.1	65	2.5	5.4	2.1	1.398
0.3	0.1	56	2.3	6.1	2.7	1.144
0.2	0.1	N/A	4.3	N/A	N/A	0.642
0.2	0.1	N/A	2.9	N/A	N/A	0.64
0.8	0.1	14	7.2	60.7	8.4	2.007
0.4	0.1	11	3.9	40.2	10.2	1.134
0.5	0.1	N/A	6.5	N/A	N/A	1.085
0.3	0.2	N/A	1.9	N/A	N/A	1.087
0.4	0.3	N/A	1.4	N/A	N/A	1.48
0.6	0.1	30	5.0	20.4	4.1	1.683
0.4	0.2	37	2.3	9.4	4.2	1.04
0.2	0.1	21	2.5	10.2	4.0	0.626
0.4	0.1	35	3.0	12.9	4.3	1.332
0.4	0.1	69	3.0	5.8	1.9	1.309
0.5	0.1	50	3.4	10.0	2.9	1.559
0.4	0.2	54	2.6	7.5	2.8	1.216
0.1	0.1	8	1.8	17.0	9.5	0.46
0.1	0.0	8	3.3	18.3	5.5	0.405
0.1	0.0	9	3.3	15.9	4.8	0.41
0.1	0.1	14	2.1	8.8	4.3	0.467
0.1	0.1	5	2.2	24.4	11.3	0.382
0.1	0.1	13	1.3	7.6	5.9	0.378

Pile Volume (m3)	Enclosed Area (km2)	α (°)	φ (°)
3.01E+06	0.394	13	2
6.27E+06	0.960	8	2
3.49E+06	0.293	13	4
1.81E+07	0.978	17	6
N/A	1.118	18	5
N/A	1.192	18	1
4.90E+06	0.450	16	5
2.40E+07	2.782	8	1
N/A	4.596	15	3
1.39E+07	1.268	18	4
1.89E+06	0.277	26	11
1.11E+06	0.177	18	5
6.15E+05	0.151	14	6
3.72E+06	0.691	18	6
5.40E+06	0.994	21	6
2.10E+07	1.921	19	2
1.52E+08	17.510	13	3
4.09E+07	3.737	25	3
1.23E+07	1.272	28	5
8.95E+07	4.926	20	2
1.07E+08	10.754	15	4
1.10E+07	1.217	14	3
1.40E+06	0.638	5	1
1.42E+06	0.237	12	5
3.30E+06	0.522	19	4
9.16E+05	0.255	20	5
5.00E+06	0.828	14	3
2.49E+06	0.495	13	3
7.77E+06	0.928	22	4
3.64E+06	0.421	26	4
8.09E+06	1.741	22	1
8.18E+06	1.139	23	5
1.15E+07	0.671	22	6
1.12E+06	0.139	16	8
4.43E+06	0.370	13	8
3.35E+05	0.440	11	5
5.75E+04	0.092	13	6
1.05E+06	0.574	15	3
6.56E+05	0.553	10	3
7.54E+06	1.597	10	3
2.02E+06	0.574	13	3
4.81E+06	4.224	10	4
4.97E+06	2.318	6	3
3.21E+06	1.622	6	4
3.95E+06	0.840	21	3
2.04E+06	0.639	13	3
1.87E+06	0.933	16	3
2.17E+06	0.757	19	4
2.61E+05	0.126	28	8

3.57E+04	0.033	25	10
7.19E+04	0.029	16	6
6.47E+04	0.033	9	3
4.95E+04	0.022	22	10
6.82E+04	0.047	11	7
1.16E+05	0.107	5	2
3.82E+04	0.048	4	2
1.83E+05	0.286	4	1
1.64E+05	0.170	5	2
2.69E+05	0.131	6	1
4.17E+04	0.043	5	1
4.24E+04	0.054	6	2
1.75E+05	0.041	23	6
7.27E+05	0.099	31	13
1.18E+05	0.020	32	17
4.69E+05	0.041	31	11
5.30E+05	0.040	31	11
8.31E+05	0.068	32	10
9.11E+05	0.102	29	10
4.79E+04	0.057	7	2
6.70E+04	0.084	7	2
7.14E+04	0.082	6	2
3.18E+05	0.835	5	0
1.19E+06	0.125	29	14
7.96E+05	0.087	33	17
7.99E+05	0.068	31	13
7.16E+04	0.017	29	20
1.33E+05	0.019	31	10
1.04E+05	0.131	5	1
4.98E+04	0.052	8	3
1.92E+04	0.042	2	2
3.62E+05	0.066	26	4
1.67E+06	0.125	31	10
1.04E+06	0.115	31	7
N/A	0.076	31	9
1.61E+05	0.024	30	7
8.77E+05	0.086	32	16
1.18E+06	0.087	32	12
1.31E+06	0.116	31	9
1.09E+06	0.083	29	11
1.21E+04	0.011	22	9
1.18E+04	0.008	21	12
1.00E+04	0.008	22	5
1.28E+04	0.008	32	18
3.98E+03	0.008	22	9
8.25E+03	0.008	34	24

Size			Sediment size class terminology	
mm	μm	ϕ	(after Friedman & Sanders, 1978)	
2048		-11	very large boulders	
1024		-10	very large boulders	
512		-9	large boulders	
256		-8	medium boulders	
128		-7	small boulders	
64		-6	large cobbles	gravels
32		-5	small cobbles	
16		-4	very coarse pebbles	
8		-3	coarse pebbles	
4		-2	medium pebbles	
2	2000	-1	fine pebbles	
1	1000	0	very fine pebbles	
0.5	500	1	very coarse sand	
0.25	250	2	coarse sand	sand
0.125	125	3	medium sand	
0.063	63	4	fine sand	
0.031	31	5	very fine sand	
0.016	16	6	very coarse silt	
0.008	8	7	coarse silt	silt
0.004	4	8	medium silt	
0.002	2	9	fine silt	
			very fine silt	clay
			clay	

Long Island

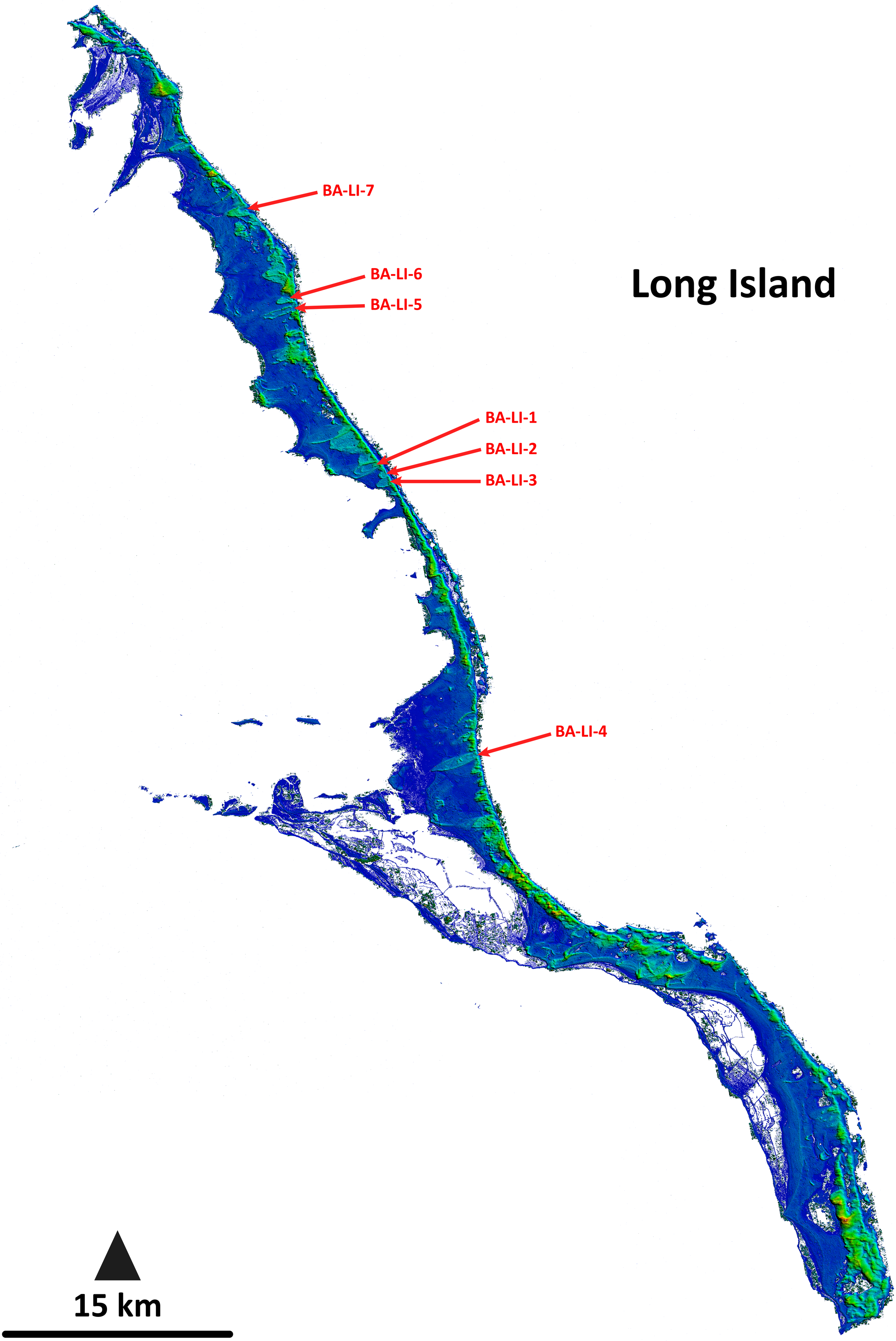

15 km

		Geometric
SAMPLE IDENTITY:	**Chevrons**	**MEAN:** 272.4
SAMPLE TYPE:	Bimodal, Moderately Well Sorted	**SORTING (s):** 1.593
SEDIMENT NAME:	Moderately Well Sorted Fine Sand	**SKEWNESS (Sk):** 0.131
TEXTURAL GROUP:	Sand	**KURTOSIS (K):** 0.927

Stats	mm	ϕ
MODE 1:	196.0	2.356
MODE 2:	327.5	1.616
MODE 3:		
D_{10}:	157.0	0.997
MEDIAN or D_{50}:	261.4	1.936
D_{90}:	500.9	2.672
(D_{90} / D_{10}):	3.192	2.679
(D_{90} - D_{10}):	344.0	1.674
(D_{75} / D_{25}):	1.946	1.683
(D_{75} - D_{25}):	183.5	0.961

GRAIN SIZE DISTRIBUT	
GRAVEL:	0.0%
SAND:	100.0%
MUD:	0.0%
V COARSE GRAVEL:	0.0%
COARSE GRAVEL:	0.0%
MEDIUM GRAVEL:	0.0%
FINE GRAVEL:	0.0%
V FINE GRAVEL:	0.0%
V COARSE SAND:	0.1%

		Geometric
SAMPLE IDENTITY:	**Aeolianites**	**MEAN:** 271.3
SAMPLE TYPE:	Bimodal, Moderately Well Sorted	**SORTING (s):** 1.542
SEDIMENT NAME:	Moderately Well Sorted Fine Sand	**SKEWNESS (Sk):** 0.228
TEXTURAL GROUP:	Sand	**KURTOSIS (K):** 1.159

Stats	mm	ϕ
MODE 1:	231.0	2.1
MODE 2:	655.0	0.6
MODE 3:		
D_{10}:	166.3	0.9
MEDIAN or D_{50}:	258.4	2.0
D_{90}:	527.3	2.6
(D_{90} / D_{10}):	3.2	2.8
(D_{90} - D_{10}):	361.0	1.7
(D_{75} / D_{25}):	1.7	1.5
(D_{75} - D_{25}):	140.4	0.8

GRAIN SIZE DISTRIBUT	
GRAVEL:	0.0%
SAND:	100.0%
MUD:	0.0%
V COARSE GRAVEL:	0.0%
COARSE GRAVEL:	0.0%
MEDIUM GRAVEL:	0.0%
FINE GRAVEL:	0.0%
V FINE GRAVEL:	0.0%
V COARSE SAND:	0.7%

		Geometric
SAMPLE IDENTITY:	**Beaches**	**MEAN:** 377.2
SAMPLE TYPE:	Polymodal, Moderately Sorted	**SORTING (s):** 1.954
SEDIMENT NAME:	Slightly Very Fine Gravelly Medium Sand	**SKEWNESS (*Sk*):** 0.254
TEXTURAL GROUP:	Slightly Gravelly Sand	**KURTOSIS (*K*):** 0.870

Stats	mm	ϕ
MODE 1:	231.0	2.1
MODE 2:	327.5	1.6
MODE 3:	655.0	0.6
D_{10}:	181.2	0.0
MEDIAN or D_{50}:	340.4	1.6
D_{90}:	983.6	2.5

GRAIN SIZE DISTRIBUT	
GRAVEL:	1.8%
SAND:	98.2%
MUD:	0.0%
V COARSE GRAVEL:	0.0%
COARSE GRAVEL:	0.0%

(D_{90} / D_{10}):	5.4	103.3
(D_{90} - D_{10}):	802.4	2.4
(D_{75} / D_{25}):	2.8	3.2
(D_{75} - D_{25}):	404.6	1.5

MEDIUM GRAVEL:	0.0%
FINE GRAVEL:	0.0%
V FINE GRAVEL:	1.8%
V COARSE SAND:	7.8%

Logarithmic	Description
1.876	Medium Sand
0.671	Moderately Well Sorted
-0.131	Coarse Skewed
0.927	Mesokurtic

ION	
COARSE SAND:	9.9%
MEDIUM SAND:	42.7%
FINE SAND:	44.2%
V FINE SAND:	3.1%
V COARSE SILT:	0.0%
COARSE SILT:	0.0%
MEDIUM SILT:	0.0%
FINE SILT:	0.0%
V FINE SILT:	0.0%
CLAY:	0.0%

Logarithmic	Description
1.882	Medium Sand
0.625	Moderately Well Sorted
-0.228	Coarse Skewed
1.159	Leptokurtic

ION	
COARSE SAND:	10.3%
MEDIUM SAND:	42.1%
FINE SAND:	45.3%
V FINE SAND:	1.5%
V COARSE SILT:	0.0%
COARSE SILT:	0.0%
MEDIUM SILT:	0.0%
FINE SILT:	0.0%
V FINE SILT:	0.0%
CLAY:	0.0%

Logarithmic	Description
1.407	Medium Sand
0.966	Moderately Sorted
-0.254	Coarse Skewed
0.870	Platykurtic

ION	
COARSE SAND:	24.3%
MEDIUM SAND:	34.3%
FINE SAND:	30.7%
V FINE SAND:	1.1%
V COARSE SILT:	0.0%
COARSE SILT:	0.0%

MEDIUM SILT:	0.0%
FINE SILT:	0.0%
V FINE SILT:	0.0%
CLAY:	0.0%